Journal of Aerospace Science and Applications

Volume No. 9

Issue No. 1

January - April 2024

ENRICHED PUBLICATIONS PVT. LTD

S-9, IInd FLOOR, MLU POCKET,
MANISH ABHINAV PLAZA-II, ABOVE FEDERAL BANK,
PLOT NO-5, SECTOR-5, DWARKA, NEW DELHI, INDIA-110075,
PHONE: - + (91)-(11)-47026006

Journal of Aerospace Science and Applications

Aims and Scope

The Journal of Aerospace Science and Applications published three issues yearly by Enriched publications. Journal of Aerospace Science and Applications is peer reviewed journal and monitored by a team of reputed editorial board members. This journal consists of research articles, reviews, and case studies on Aerospace Research. This journal mainly focuses on the latest and most common subjects of its domain.

Authors are invited to submit papers on new advances in the following topics to aerospace applications:

- Materials and structures
- Flight mechanics
- Navigation, guidance and control
- Electromagnetism and radar
- Signal and image processing
- Information processing
- Human behaviour
- Robotics and intelligent systems

Journal of Aerospace Science and Applications

Managing Editor
Mr. Amit Prasad

Journal of Aerospace Science and Applications

(Volume No. 9, Issue No. 1 January - April 2024)

Contents

Experimental Investigation of The Performance Characteristics of A Spark Ignition Engine By Varying The Compression Ratio

P. Goyal[1], S.K. Sharma[2‡], Amit Pal[3]

[1]Amity Institute of Aerospace Engineering, Amity University Uttar Pradesh, India
priyankagoel03@gmail.com

[2]Quality Assurance Enhancement Department, Amity University Uttar Pradesh, India
Sks15nov@gmail.com

[3]Department of Mechanical Engineering, Delhi Technological University, Delhi, India
amitpal@dce.ac.in

[‡]Corresponding Author; Tel: +91 8800987446

ABSTRACT

The Spark Ignition Engine has been extensively used in various sectors viz. Automobile industries, etc. In today's scenario, there is a huge need to improve the performance characteristics of the spark ignition engine. Compression ratio is a major factor which plays an important role in the spark ignition engine and it has a greater influence also on the performance characteristics of an internal combustion engine. The present research paper shows an experimental investigation of the effect of compression ratio on the performance characteristics which are brake power, brake thermal efficiency, brake mean effective pressure and specific fuel consumption of the spark ignition engine. Different compression ratios with different engine speeds were used in the present study. This work shows that there is a remarkable decrement in the specific fuel consumption with an increased compression ratio and improved brake power, brake thermal efficiency and brake mean effective pressure.

Keywords - *Spark Ignition engine; compression ratio; engine speed; brake power; specific fuel consumption.*

1. Introduction

Improving efficiency of an Internal Combustion Engine is a major concern in today's fast growing automobiles sector. Higher compression ratio is one of the very useful and important aspects to improve the fuel consumption and power output in gasoline engines as combustion efficiency increases with the compressed air and fuel mixture [1]. Most of the energy produced by these engines lost in the form of heat. There is a number of other losses also associated with the engine like friction losses and losses of the exhaust and some other parameters which also affects the thermal efficiency of the engine [2,3,4].

Compression Ratio (CR) is the ratio of the total volume of the combustion chamber when the piston is at bottom dead centre to the total volume of the combustion chamber when the piston is at top dead centre [5]. Lots of research has been devoted to the effect of the higher compression ratio of a spark ignition engine.

The main challenge is that the conventional gasoline engines operate at an optimal compression ratio, which is set low enough to prevent premature ignition of the fuel, or knock, at high power levels under fast acceleration, high speeds or heavy loads. But, most of the time, gasoline engines operate at relatively low power levels under slow acceleration, lower speed, or light loads.

VCR Engine

A variable compression ratio (VCR) engine is able to operate at different compression ratios, depending on the particular vehicle performance needs. The VCR engine is optimized for the full range of driving conditions, such as, acceleration, speed and load. At low power levels, the VCR engine operates at high compression to capture the benefits of fuel efficiency, while at high power levels, it operates at low compression levels to prevent knock. To further improve the fuel economy, the VCR engine is small, with about one-third the displacement volume of a conventional gasoline engine [6].

VCR Concepts

Conventionally, every mechanical element in the power conversion system has been considered a way to achieve a variable compression ratio. Many designs presented solved by various researchers which modifies the compression ratio by the following methods [7]:

- Moving the cylinder head;
- Variation of combustion chamber volume;
- Variation of piston deck height;
- Modification of connecting rod geometry;
- Moving the crankshaft axis;

In many cases, the deviation from conventional production engine structure or layout represents a significant commercial barrier to wide spread adoption of the technology.

Applications of VCR Engines

The concept of a variable compression ratio promises improved engine performance, efficiency and reduced emissions also [6,7].

- Higher compression ratio gives faster laminar flame speed. Therefore, the ignition delay period is shorter. As a result, at low loads, the greater the compression ratio, the shorter is the combustion time. Time loss is subsequently reduced. Therefore, it seems reasonable that fuel consumption rate is lower with high compression ratios at part load.

- The VCR can make a significant contribution to thermodynamic efficiency. A VCR engine can continuously vary the compression ratio by changing the combustion chamber volume. In a VCR engine, thermodynamic benefits appear throughout the engine map.
- The optimum compression ratio is determined as a function of one or more vehicle operating parameters such as inlet air temperature, engine coolant temperature, exhaust gas temperature, engine knock, fuel type, octane rating of fuel etc. In a VCR engine, the operating temperature is more or less maintained at optimum, where combustion efficiency is high.

This paper specifically discusses the effect of a variable compression ratio on the performance characteristics of a spark ignition engine. One researcher conducted a research on the effect of the higher compression ratio in two-stroke engines and showed that the actual fuel consumption was improved by 1-3% for each unit increment in the compression ratio [8]. Power output also improves, but the maximum compression ratio is limited because of the knock and the thermal loads. It was also noticed that the rate of improvement was lesser compared with the theoretical values. But these redundancies were due to the mechanical, cooling losses and mainly due to the thermal losses which were explained above. Similarly, experiments performed on four-stroke a petrol engine which also shows the remarkable increment in the mechanical efficiency and thermal efficiency of a spark-ignition engine [9,10].

2. Experimental Set-up

The schematic diagram of the experimental setup is shown in Fig. 1. The performance characteristics like brake power, brake thermal efficiency, brake mean effective pressure and specific fuel consumption have been measured with varying compression ratio of 5 to 9 at different engine speed of 1300 to 1600 RPM with the each increment of 100rpm of a spark ignition engine. The specifications of the test engine are shown in Table 1.

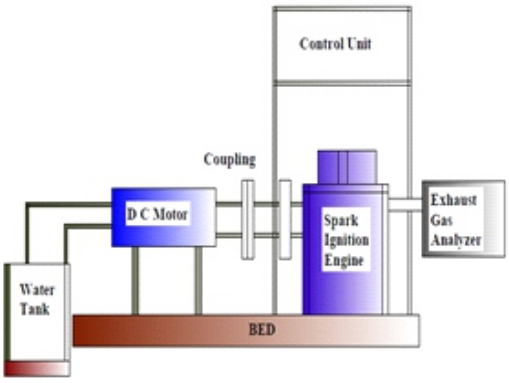

Fig. 1. A systematic layout of test setup

Table 1. Specification of the Experimental Set up

Item	Specification
Engine Type	Single Cylinder 4 Stroke Engine
Fuel	Gasoline
Cooling system	Water cooled
Stroke (mm)	110
Bore (mm)	80
Compression ratio	9.2:1
Spark variation range	0-70 btdc
Type of Injection	Direct Injection
Injection Pressure (bar)	200
Load Indicator	Digital, range 0-50 kg, supply 230V, AC

3. Results And Discussion

The following graphs were obtained by the experimental analysis for brake power, brake thermal efficiency, brake mean effective pressure and specific fuel consumption by varying the compression ratio at different engine speed.

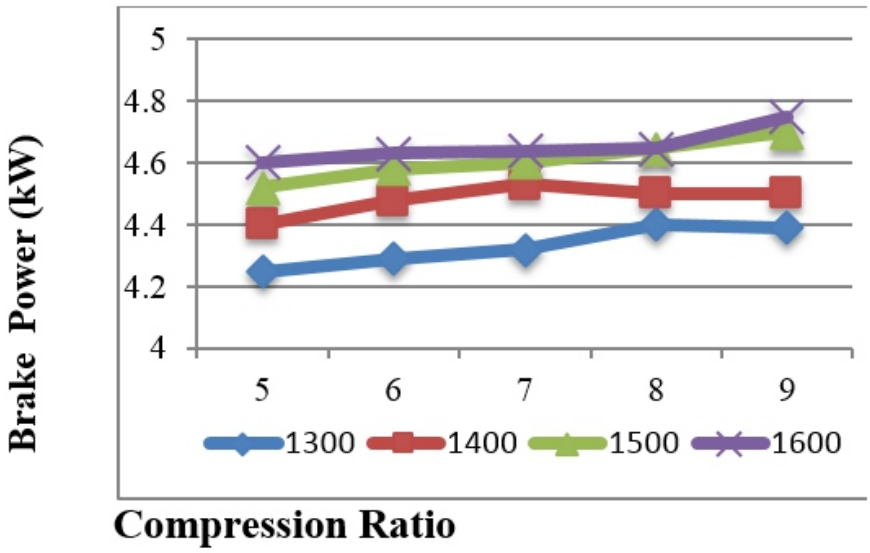

Fig. 2. Variation of brake power with compression ratio at different engine speed.

Brake Power (kW): In the comparative analysis of brake power with compression ratio of different engine speed as shown in Fig 2. It is observed that brake power increases with the compression ratio. This is mainly due to the increase in brake torque at high compression ratios. Engine torque is directly related to brake power which is a theoretical fact. Therefore, as the engine gives more push on the piston, and then more torque is generated.

Brake Mean Effective Pressure (bar): In the comparative analysis of brake power with compression ratio of different engine speed as shown in Fig. 3. It is observed that brake mean effective pressure increases with the compression ratio. But the lowest increase in the pressure occurs at the 1400 RPM and it is more or less constant from the compression ratio 6 to 9 at engine speed of 1400 RPM. The highest increment in the pressure occurs at a compression ratio of 9.

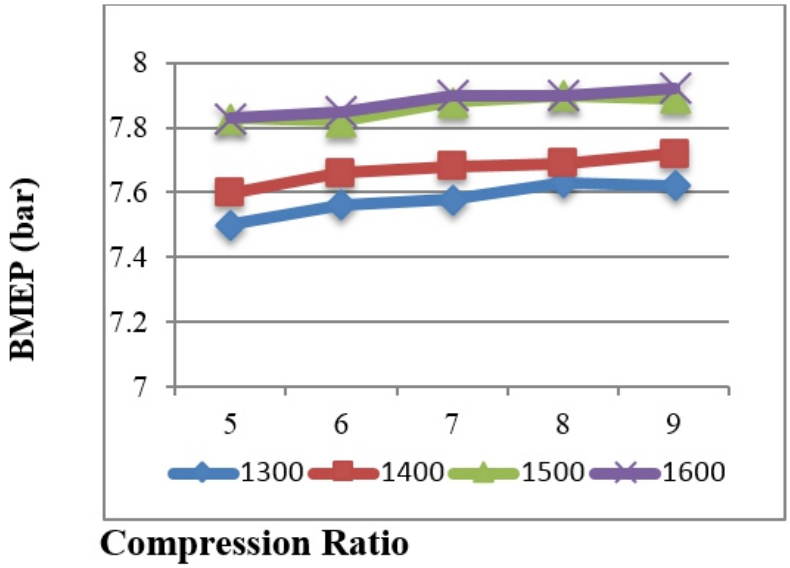

Fig. 3. Variation of brake mean effective pressure with compression ratio at different engine speed.

Brake Thermal Efficiency (%): In the comparative analysis of brake thermal efficiency with compression ratio of different engine speed as shown in Fig. 4. The graph clearly shows that the brake thermal efficiency is maximum at a higher compression ratio. Better mixing and evaporation of the fuel occurs with the greater compression of the available fuel and air. As the compression ratio increases, combustion efficiency also increases, which results in the remarkable increment in the energy also.

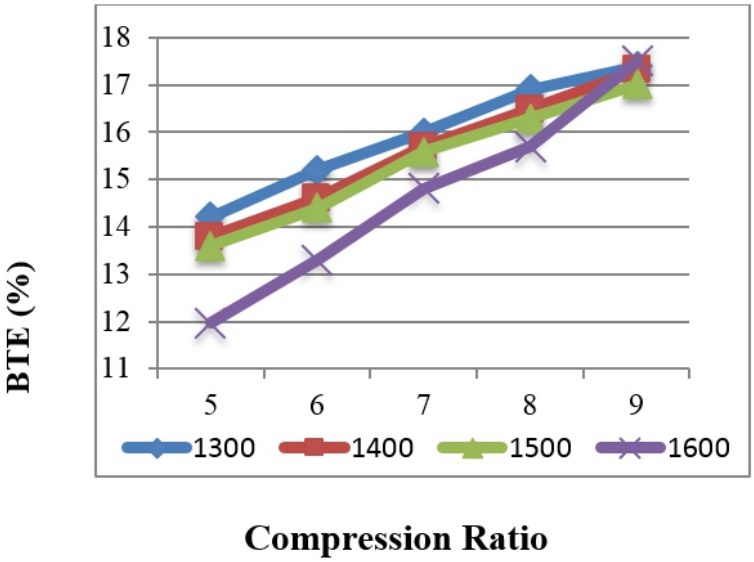

Fig. 4. Variation of brake thermal efficiency with compression ratio at different engine speed.

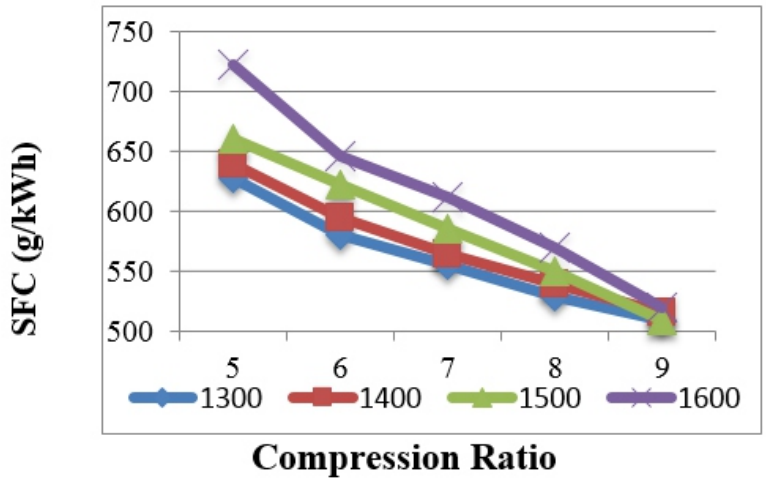

Fig. 5. Variation of specific fuel consumption with compression ratio at different engine speed.

Specific Fuel Consumption (g/kWh): In the comparative analysis of specific fuel consumption with compression ratio at different engine speed as shown in Fig. 5. It is shown that the less fuel is required at higher compression ratios as the fuel mixture is effectively compressed which causes the higher thermal efficiency. Resultin the reduced fuel consumption at higher compression ratio.

4. Conclusion

As from the above result, we can conclude that the increase in the compression ratio improves the overall efficiency of an engine. It also improves the fuel consumption with the each unit of increment in the compression ratio. Brake thermal efficiency shows the increment of 3-6% for each unit increase of

compression ratio. Brake power, brake mean effective pressure also shows a remarkable increment for the higher compression ratio. There is a considerably higher difference in the theoretical and experimental results which is primarily because of the thermal, mechanical and frictional losses. To further enhance the efficiency of an engine alternative fuels are the best option with the higher compression ratio and can be incorporated with the number of different design parameters.

References

Andreas, B., "Torque Modeling and Control of a Variable Compression Engine", Dept. of Electrical Engineering at Linkopings University, Sweden. 2003. (Master's Thesis)

[1] *David Gerard, Magali Besson, Marc Thomine "HCCI combustion in a diesel VCR engine" SAE 2008-01-1187 April 14th 2008.(Article)*

[2] *F.H Palmer, "Vehicle performances of gasoline containing oxygenates", International conference on petroleum based fuels and automotive applications, London, UK; pp. 33–46, 1986.(Conference Paper)*

[3] *Maurillio, Marco Lucio, Sergio Gradella Villalva "Variable compression ratio engines" SAE 2009-36-0245 October 10th 2009. (Article)*

[4] *Heywood J. B., Internal combustion Engines Fundamentals. McGraw Hill Book Company, pp.450-458, 1988. (Book)*

[5] *R G Sykes,Tickford, Engines Expo 2000 paper, "Methods to reduce the fuel consumption of gasoline engines". (Conference)*

[6] *J R Clarke, R J Tabaczynski, US Patent 6135086,2000-10-24, "Internal combustion engine withadjustable compression ratio and knock control". (Patent)*

[7] *Yuh, M. and Tohru, G., 2010, "The Effect of Higher Compression Ratio in Two-Stroke Engines", Yamaha MotorCo, Ltd. pp 355-362. (Article)*

[8] *Rychter T.J., Teodorczyk A., Stone C.R., Leonard H.J., Ladommatos N. and Charlton S.J. "A theoretical study of a variable compression ratio turbocharged diesel engine".Vol.206, Part A: Journal of Power and Energy, 1992, pp.227-238. (Article)*

[9] *C.L. Song, W.M. Zhang, Y.Q.Pei, G.L.Fan, G.P.Xu, "Comparative effect of MTBE and ethanol addition into gasoline on exhaust emission", Atmospheric environment, pp. 403-410,2006.(Article)*

SDR Joint GPS / Galileo Receiver From Theory To Practice

Mr. Sanjay Kumar

A B S T R A C T

This paper deals with a Software Defined Radio (SDR) receiver capable to process GPS and Galileo signals jointly. A large set of possible solution can be implemented, with the main aim of assessing the performance of the receiver for the considered architectures. For this reason, software receivers, either real-time or non-real-time, are fundamental tools to enable research and new developments in the field of GNSSs. In this paper our intent is to discuss some of the choices one can face when implementing an SDR GNSS receiver, switching from the theory to the practice. We focus our attention on the pseudorange construction and the Position, Velocity and Time (PVT) estimation stage, discussing different algorithms to implement these blocks. Our aim is to offer an insight on the options to implement those stages of the receiving chain, in a practical vision which is difficult to find in the available literature.

Keywords: Software Defined Radio, Gnss Software Receiver, Galileo, Gp

1. Introduction

In recent times, particular attention has been directed toward the development of new Global Navigation Satellite Systems (GNSSs), as the European Galileo and the renewed Russian GLONASS. All these systems aim to be interoperable each other and with the GPS, and to be exploited all at once, to provide the user receiver with a large set of measurements, entailing better precision and robustness[1][2].

Software Defined Radio (SDR) is a modern technology that allows to replace part of the hardware of a radio device with a software architecture running on an appropriate digital processor[3][4][5][6]. Such an approach allows the development of reconfigurable terminals, thanks to the ease of access to every single functional block implemented in software. This characteristic happens to be very useful for system designers that are provided with a valuable tool for testing and comparing algorithms and architectures, quickly implemented as simple software modules.

In this article we discuss the possibility to implement a SDR receiver capable to jointly process both the GPS and Galileo signals. In particular, we discuss some of the issues that may commonly arise in designing a joint GPS/Galileo software receiver for research purposes, taking as an example our real-time software receiver, N-Gene[7].

Although abundant literature is available on architectures and algorithms for GNSS receivers (see for example[8]—[17] and references therein), it is often difficult and time-consuming to cope with the implementation options arising when passing from the theory to the practice, as it can be seen even in the recent literature and research activities[15] —[18].

We discuss here implementation choices related to the tracking stage and to the Position Velocity Time (PVT) computation, since these are in our opinion the characterizing blocks in a joint GPS/Galileo receiver, when processing measurements from Galileo and GPS at the same time. Since the Galileo signal is not currently available, our tests relied on the signals produced with the Spirant GSS7700 and GSS7800 generators.

The remainder of the paper is structured as follows: in Section II we discuss the architecture of the receiver: subsection A introduces the acquisition stage, while subsections B and C describe in details the tracking and PVT stages, emphasizing the issues that arise when dealing with a joint GPS/Galileo receiver. In Section III we show some results obtained processing the data collected using the Spirent signal simulators, comparing the results obtained using the different considered algorithms. Finally, in Section IV we draw the conclusions of this work

2. Receiver Architecture

As one of the goals of the software receiver we consider in this paper is to be a research and investigation tool, its basic architecture, shown in Figure 1, is represented using a standard "educational" design, made up by the typical modules that constitute a GNSS receiver blocks chain. The shaded area represents the functionalities implemented in software from the Analog-to-Digital Converter (ADC) on. The overall software module resides on a PC and works in real-time with respect to the signal output by the ADC. The signal processing executed by the Backend Section (opposite to the Frontend one, in the SDR language) after the Analog toDigital Converter (ADC) consists of several actions.

Signal acquisition, in order to roughly align the received code with the internal replica; tracking of the received code and carrier, in order to align the incoming and local spreading codes, finely removing the frequency shifts due to the Doppler effect.

Demodulation of the navigation data, in order to recover the ephemera is information, retrieve the satellite's position and calculate the time offset between the satellite and system time. All the information regarding the data structure of both the Galileo and GPS can be found in[19] and[20] respectively; measurement of the code phases from the PRN sequences of the satellite signals, in order to estimate the pseudo ranges; PVT computation in order to estimate the user's position.

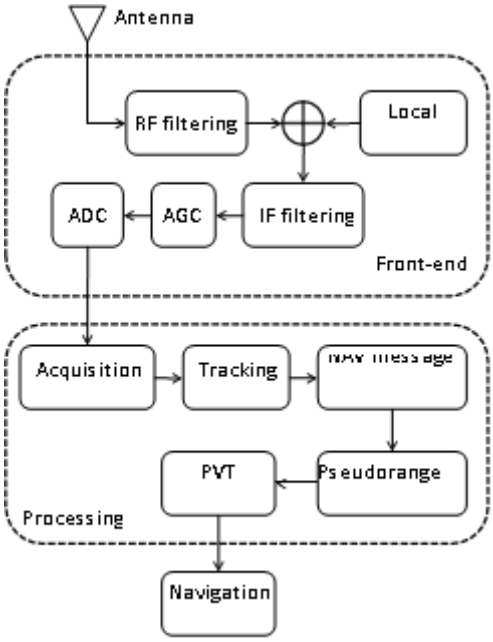

Figure 1. Architecture of the considered software receiver

2.1. Acquisition Stage

In order to track and decode the information transmitted by the GNSS constellation, a generic receiver must at first detect the presence of the signal in space, performing the acquisition. The receiver must be able to search over a certain frequency range in order to cover all the expected Doppler frequency shifts on the received signal Once the acquisition algorithm detects the presence of the signal, two parameters must be estimated

- the *delay* τ of the received code with respect to the local code,
- the *Doppler frequency shift* f_d of the received signal (due to the relative velocity between the transmitting satellite and the user receiver).

The search space for acquisition operations must cover the full range of uncertainty in the code and Doppler offset. There are different methods to perform acquisition, based on the evaluation of the cross-correlation function of the received signal with a local signal, generated for each value of delay τ

and Doppler shift f_d under evaluation (Cross-Ambiguity Function, CAF). Serial search (i.e., the cell-by-cell evaluation of the 2-dimensional CAF) is suitable for hardware receivers, due to its simplicity in implementation. Instead, in the perspective of a fully-software implementation, we focus on the parallel search in frequency domain, which exploits the Fast Fourier Transform (FFT), while serial search method is extremely slow for software-based implementation[21][22].

Indeed, methods based on FFT can be used to efficiently evaluate the correlation function. In the hypothesis to observe one code period (pre-detection integration T_{int} time equal to the code period T_c), the incoming sampled signal $s_{in}[n] = s_{in}(nT_s)$ (where the sampling time T_s is chosen according to the GNSS signal specifications), is FFT-transformed, obtaining the sequence $S_{in}[m] = S_{in}(m/T_s)$= FFT$\{s_{in}[n]\}$.

A period of the current spreading code x is generated by the local code generator and it is stretched according to all the possible Doppler bins i, taking into account the minimum frequency resolution imposed by the time of observation T_{int}. The obtained signals are FFT-transformed, obtaining the sequences in the frequency domain.

The multiplications are then computed for each couple (x,i) in the frequency domain. After that, the inverse FFT (IFFT) is performed, so obtaining the circular correlation sequence. Its absolute value is computed and a possible peak in the delay domain is searched. This allows evaluating the relative delay of the spreading code for a certain Doppler shift step I.

This procedure has been performed to acquire both GPS and Galileo satellite signals. Of course, the code period T_c is different between the aforementioned GNSS signals. In case of E1-B this procedure has been performed to acquire both GPS and Galileo satellite signals. Of course, the code period T_c is different between the aforementioned GNSS signals. In case of E1-B Galileo signal we have a code length equal to 4ms as reported in[19] while the T_c in case of L1 C/A for GPS is 1ms[20].

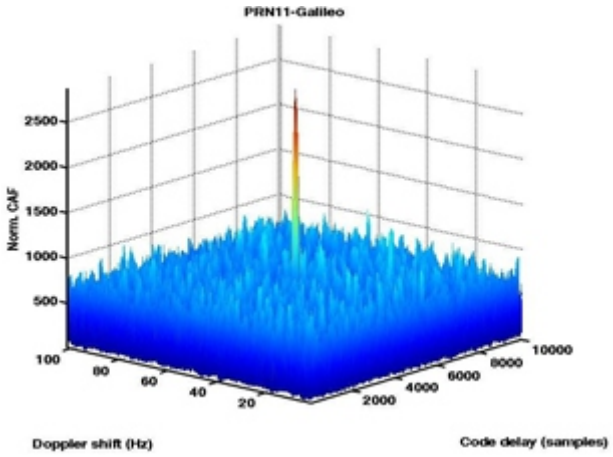

Figure 2. Estimated CAF for Galileo PRN 11

The CAF obtained by using the latter acquisition technique to process the Galileo PRN 11 is shown in Figure 2.It is possible to identify a peak in the search space and it corresponds to the Maximum-Likelihood (ML) estimate of the Doppler shift and code delay. Such a method is well suited to be implemented in a real-time software receiver. For example, the N-Gene receiver is able to perform in parallel the initial acquisition of all the four satellite channels necessary for the first PVT fix.

2.2. Tracking Stage and Pseudo range Computation

Once the acquisition phase has brought the received and the locally generated code within less than a half chip period residual offset, a fine synchronization, named tracking, takes over and keeps the two codes aligned, by means of closed loop operations. Generally, the tracking system in GNSS receivers consists of a Delay Lock Loop (DLL) for code tracking and a Phase Lock Loop (PLL) for carrier phase tracking.

A detailed analysis of how a PLL and DLL work is out of scope of this paper and an exhaustive description can be found in[21]. The main aim of this Section is to stress the fundamental role played by the tracking stage in the correct and precise recovery of the code delay τ, which is necessary to measure the pseudo ranges, and consequently the PVT solution, and to decode the navigation message. Focusing on the estimation of the pseudo ranges, they are usually computed using two different methods.

1) The first technique (named common transmission time) is based on the satellites transmission time. In fact, all satellites broadcast data synchronously but, due to different propagation delays, at a given time the user does not receive the same data from every satellite.

Once each preamble is identified for all available channels, a comparison on their time of arrival is performed. In this case, in order to determine the set of pseudo ranges for the first time, the channel with the earliest arriving sub frame is assumed as a reference and a minimum travel time is assigned to the reference channel (e.g., its value, for GPS, is in a range between 65 and 85 ms). This concept is sketched in Figure 3.

All other pseudo ranges are then derived respect to the reference channel through proper time counters, that are continuously updated by the tracking structures of each channel. If we suppose that the start of the sub frame is identified for all the tracked satellites, then the receiver measures the time difference between the starting points of the sub frame and the reference one. This time difference δ_i can therefore been written as $\delta_i = t^R_{rx,i} - t^R_{rx,1}$, where $t^R_{rx,i}$ represents the time of reception of the subframe for the i-th satellite while $t^R_{rx,1}$ is the time relative to the reference satellite.

The time difference δ_i for each i-th satellite can be computed by means of specific time counters. Although there are many time-keeping conventions, which depend on the specific receiver implementation, the system of counters has to accumulate the number of words (i.e.: in case of the GPS C/A code, 1 word = 0.6 s), data bits (i.e.: 1 data bit = 20 ms), code periods (i.e.: 1 GPS C/A code period = 1 ms), and samples (i.e.: 1 sample = 1/sampling frequency f_s) In the case of Galileo, the procedure is similar to the GPS case. The receiver has to store the following parameters, in order to compute a valid pseudorange: number of pages (i.e.: 1 page = 2 s), data bits (i.e.: 1 data bit = 4 ms), code periods (i.e.: E1-B code period = 4 ms) and samples (i.e: 1 sample = 1/sampling frequency where f_s is the same as the GPS's one, as the receiver uses a unique front end to collect and digitalize the incoming GNSS signals). It is important to stress that re-ceivers are able to measure the time offset with a resolution on the order of a fraction of chip (i.e.: a fraction of micro-seconds).

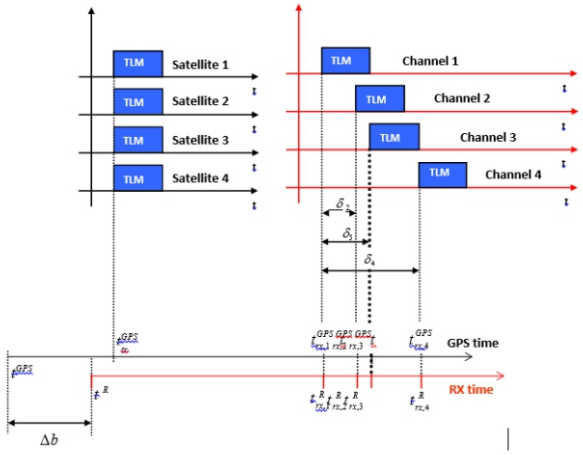

Figure 3. Pseudorange computation based on transmission time

With these time differences, the pseudoranges can be written as $\rho_i = \rho_1 + c\Delta b + c\delta_i$, where Δb is the bias between the clock of the user and the ones on board of the satellites, c is the speed of light, ρ_1 is the pseudorange relative to the reference channel and δ_i is the delay of the i-th satellite channel with respect to the reference satellite.

This kind of approach has some disadvantages to be implemented in a real-time fully software receiver:

(a) Since the beginning of a given subframe transmitted by different satellites is received at different times, the receiver has to count for each tracked satellite the time elapsed from the reception of the subframe in the reference channel (i.e. the satellite with the shortest distance to the user's receiver) to the beginning of same subframe for at least other three satellites. As a consequence, this kind of approach is not particularly suitable in a real-time implementation, since it requires to wait until all the channels have received the same data bit (e.g. the beginning of the same subframe) to compute the pseudoranges.

(b) In case of a joint GPS/Galileo scenario, this technique is unsuitable in real-time implementations, since the receiver would have to work with two independent satellite systems, characterized by different data structures and two separate reference channels (one for GPS and one for Galileo). This approach will force the receiver to keep a large amount of information into its buffer, with a significant waste of resources as well as a non-negligible delay in the PVT computation. For this reason, it is useful to consider a different method, that takes into account the status of every channel at a given, unique time, fixed by the receiver.

(2) The second approach (*common reception time*) performs the pseudoranges estimation by setting a common reception time over all the channels. In this case, which is sketched in Figure 4, the time elapsed from the reference bit (TLM in the Figure) to the bits currently considered in each channel (X, Y, Z, W in the Figure) is different for each channel, since the transmission time corresponding to the data message currently processed by the receiver is different for all the satellites.

The different time offsets are computed measuring the time passed from the reception of the last subframe and the receiving time instant set by the receiver as shown in Figure 4.

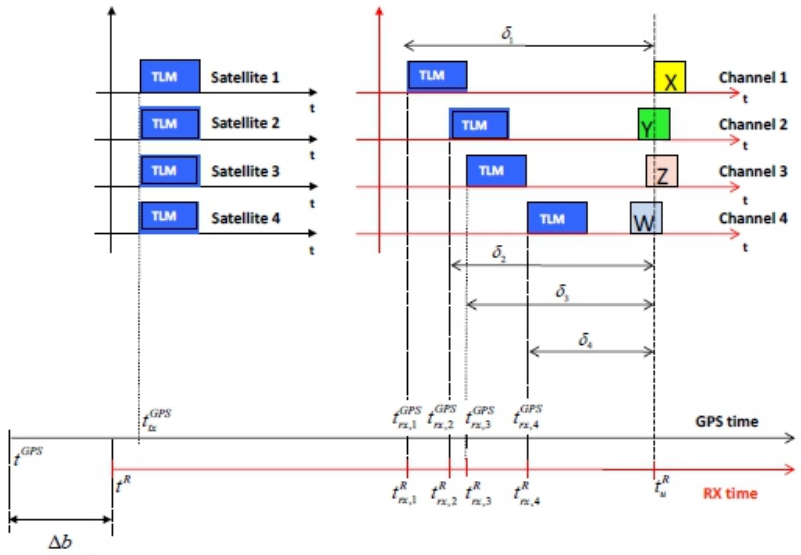

Figure 4. Pseudorange computation based on transmission time

Also in this case, the channel with the lowest time counter is selected as the reference and its propagation delay is generally chosen in a range between 65 and 85 ms. All other channels will have a longer propagation delay, proportional to their distances. In this case, the time difference δ_i can be computed as $\delta_i = t^R_{rx,i} - t^R_u$, where t^R_u, is the time when the receiver computes the pseudoranges and it is common to all the tracked signals.

This method allows to obtain pseudoranges at any time, without waiting for a particular bit front on each channel, and it is often employed in commercial GPS receivers and is the technique that has been implemented in our joint GPS/Galileo receiver.

The effect on the final PVT accuracy of implementing these two approaches will be analyzed in Section III.

2.3. PVT Computation

The computation of the PVT can be demanded to many different algorithms. Nonetheless, this stage must be always provided with the following data, at least:

- Pseudorange measurements
- Doppler measurements
- Satellites related data (positions, errors, etc.)

The simplest method to implement the PVT stage of a GNSS receiver is to consider the Least Squares (LS) solution [21]. The rationale is to iteratively update the position solution at a given time, starting from a generic linearization point (usually the centre of the earth) and iteratively updating it to converge to the least squares estimate given by the current set of measurements. The linear equation stating the relation between the pseudorange prediction error vector, $\Delta\rho$, and the estimated position error, Δx, is the following:

$$\Delta\boldsymbol{\rho} = \begin{bmatrix}\Delta\boldsymbol{\rho}_{\mathrm{GPS}} \\ \Delta\boldsymbol{\rho}_{\mathrm{Gal}}\end{bmatrix} = \mathbf{H}_{pdr}\,\Delta\mathbf{x}$$
$$= \begin{bmatrix}\boldsymbol{a}_{x,GPS} & \boldsymbol{a}_{y,GPS} & \boldsymbol{a}_{z,GPS} & \mathbf{1} & \mathbf{0} \\ \boldsymbol{a}_{x,Gal} & \boldsymbol{a}_{y,Gal} & \boldsymbol{a}_{z,Gal} & \mathbf{0} & \mathbf{1}\end{bmatrix}\Delta\mathbf{x}$$

where $\Delta\rho$ is the difference between the measured and estimated pseudoranges, Δx is the correction to be applied to the linearization point and the matrix $\mathbf{H}_{pdr}$ is the Direction Cosine Matrix (DCM), whose rows are made up by the unitary vectors pointing from the linearization point toward each one of the satellites in view; the subscript *pdr* stands for 'pseudorange'.

It must be noted that the pseudorange prediction error and the DCM are conceptually made of two parts. The upper part stores the values related to the GPS measurements, while the lower part stores the measurements related to Galileo. Moreover, the vector Δx is made up by five elements:

$$\Delta\mathbf{x} = [\Delta x \quad \Delta y \quad \Delta z \quad \Delta\tau_{GPS} \quad \Delta\tau_{Gal}]^{\mathrm{T}}$$

where the first three components are the corrections in meters to be applied to the ECEF components of the linearization point, the last two are the clock bias corrections in meters to be applied to the GPS and Galileo clock bias linearization point, since the receiver must take into account a clock bias with respect to the GPS (upper part) and a clock bias with respect to Galileo (lower part), and T points out the transpose of the vector.

A similar result is obtained for the prediction of the velocity, when Doppler measurements are exploited [21]. In this case, the clock drift is the same for both the GPS and Galileo, so that the measurement matrix shows four columns:

$$\mathbf{H}_{dop} = \begin{bmatrix}\boldsymbol{a}_{x,GPS} & \boldsymbol{a}_{y,GPS} & \boldsymbol{a}_{z,GPS} & \mathbf{1} \\ \boldsymbol{a}_{x,Gal} & \boldsymbol{a}_{y,Gal} & \boldsymbol{a}_{z,Gal} & \mathbf{1}\end{bmatrix}$$

and the corrections vector to the estimated velocity has four components:

$$\Delta\dot{\mathbf{x}} = [\Delta v_x \quad \Delta v_y \quad \Delta v_z \quad \Delta v_\tau]^{\mathrm{T}}$$

where the first three components are the ECEF corrections in meters per second and the last component is the local clock drift correction in meters per second; the subscript dop stands for 'Doppler'. The linear relationship between the pseudorange-rate error vector, $\Delta\rho$, and the estimated velocity error is then

$$\Delta\dot{\boldsymbol{\rho}} = \mathbf{H}_{dop}\,\Delta\dot{\mathbf{x}}$$

Whenever a PVT solution has to be delivered, the LS iterations run to resolve the two linear systems written above.

Despite this method is simple, it has two main drawbacks. The first one is due to the complexity, since for each point the algorithm must usually iterate until the corrections are below a threshold and each time the pseudo-inverse matrix of $\mathbf{H}_{pdr}$ (and $\mathbf{H}_{dop}$) must be computed. This issue might be avoided introducing a model to make the linearization point evolve, as in a Kalman filter.

The second drawback of the LS approach is due to the fact that the estimate is computed only on the basis of the current measurements, without any regards to the past trajectory and without weighting the available measurements. Despite the atter issue is solved using the Weighted LS (WLS), it is not possible to cope with the past trajectory using a LS-based method, ince it has no memory and at each time a solution is computed independently from the past.

For this reason, it is useful to adopt other methods that rely on the representation of state-space models [23]—[26]. Among these, the algorithm that historically has shown the best compromise between performance and complexity in GNSS receivers is the Extended Kalman Filter (EKF) [26], which is characterized by the following state-space equations:

$$\begin{aligned} \Delta\mathbf{x}[n+1] &= \mathbf{F}\Delta\mathbf{x}[n] + \mathbf{w}[n] \quad \text{state equation} \\ \Delta\mathbf{z}[n] &= \mathbf{H}[n]\Delta\mathbf{x}[n] + \mathbf{v}[n] \quad \text{measurement eq.} \end{aligned}$$

where $\Delta\mathbf{x}$ is the incremental state, $\mathbf{F}$ is the state transition matrix, $\Delta\mathbf{z}$ is the measurement prediction error, $\mathbf{H}$ is the measurement matrix, $\mathbf{w}$ is the process noise and $\mathbf{v}$ is the measurement noise. The notation is in part similar to the one adopted in the LS discussion. This is a voluntary choice, since the two algorithms are based upon similar concepts. The incremental states represent the increments (corrections) to be applied to an a priori estimate $\bar{\mathbf{x}}[n+1]$ of the state, which acts as a linearization point. The state model adopted here is characterized by nine incremental states, the first five related to position and the last four related to velocity:

$$\Delta\mathbf{x} = \left[\Delta x, \Delta y, \Delta z, \Delta\tau_{GPS}, \Delta\tau_{Gal}, \Delta v_x, \Delta v_y, \Delta v_z, \Delta v_\tau\right]^T$$

to which the following state-transition matrix is associated:

$$\mathbf{F} = \begin{bmatrix} 1 & 0 & 0 & 0 & 0 & T_s & 0 & 0 & 0 \\ 0 & 1 & 0 & 0 & 0 & 0 & T_s & 0 & 0 \\ 0 & 0 & 1 & 0 & 0 & 0 & 0 & T_s & 0 \\ 0 & 0 & 0 & 1 & 0 & 0 & 0 & 0 & T_s \\ 0 & 0 & 0 & 0 & 1 & 0 & 0 & 0 & T_s \\ 0 & 0 & 0 & 0 & 0 & 1 & 0 & 0 & 0 \\ 0 & 0 & 0 & 0 & 0 & 0 & 1 & 0 & 0 \\ 0 & 0 & 0 & 0 & 0 & 0 & 0 & 1 & 0 \\ 0 & 0 & 0 & 0 & 0 & 0 & 0 & 0 & 1 \end{bmatrix}$$

Each time a new set of pseudorange and Doppler measurements is available, the Kalman filter is iterated once. The first step (*prediction*) allows to get the a priori estimate $\mathbf{x}^{-}[n+1]$ by using the last obtained estimate of the PVT in the state equation. This value is used to compute the prediction of the measurements and, together with the measurements, to compute the correction to be applied to the a priori estimate, as follows (update):

$$\Delta\mathbf{x}[n+1] = \Delta\mathbf{x}[n] + \mathbf{K}[n](\Delta\mathbf{z}[n] - \mathbf{H}[n]\Delta\mathbf{x}[n])$$

where $\mathbf{K}[n]$ is the Kalman gain. Finally, the *a posteriori* estimate $\mathbf{x}^{+}[n+1]$ is obtained correcting the a priori estimate:

$$\mathbf{x}^{+}[n+1] = \mathbf{x}^{-}[n+1] + \Delta\mathbf{x}[n+1]$$

The main advantage of the EKF with respect to the LS is the introduction of a method to balance the contribution of the trajectory given by the model and the one obtained by the measurement. In this way, it is possible to obtain a smoother trajectory than the one obtained using the LS and to avoid the model trajectory to diverge. A complete definition of this model can be found in [26] and [27]. These results will be analyzed in the following section.

3. Comparative Results

In this Section we investigate the effects of the two different approaches to compute the pseudoranges discussed in Section II.B; then, we show some results we obtained by using both a LS and an EKF approach to resolve the PVT problem.

Concerning the calculation of the pseudoranges, an example of their estimation results by using the two methods of Section II.B is depicted in Figure 5, taking as an example the GPS satellite with PRN 30.

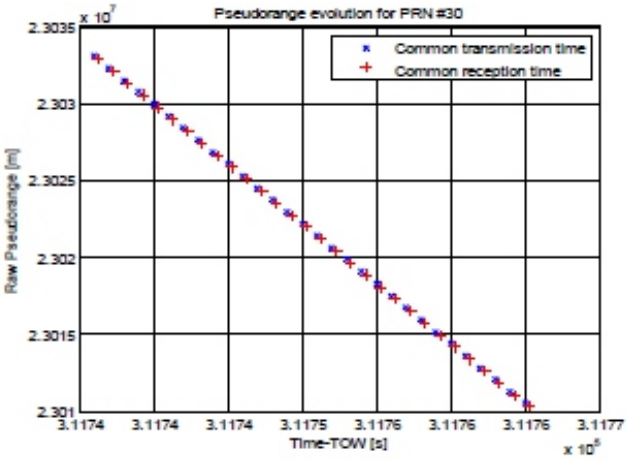

Figure 5. Comparison between pseudoranges computed by using common reception time and common transmission time

The blue 'x's represent the pseudorange computed by considering that all the satellite broadcast the same navigation data at the same Time of Week (TOW) (*common transmission time*). On the contrary, the red '+'s show the pseudorange as calculated by fixing a unique time of reception, that is set internally by the receiver (*common reception time*); as a consequence, the time of transmission of the navigation data is different for each satellite. Therefore, if we suppose to start the PVT computation at the beginning of a subframe and to update it every second, the pseudorange computed using the first method is measured when the time of transmission is equal to TOW. In the second case the pseudorange is computed at a transmission time that is not the same as TOW, but changes according to the reception time that has been fixed in the receiver. As discussed before, this latter approach allows to simplify the state-machine governing the operations of the receivers, as well as to reduce the memory occupied for the satellite channels in tracking.

In order to clarify this concept, in the two columns of Table I we show the TOW of the bit sampled in the reference channel, considering both the common transmission time and the common reception time methods.

Table 1. Transmission time of the considered bit front

TIME OF TRANSMISSION[s]	
Common transmission time	*Common reception time*
311736	311736.277662467
311737	311737.277664239
311738	311738.27766595
311739	311739.277667661
311740	311740.277669371
311741	311741.277671082
311742	311742.277672854
311743	311743.277674503
311744	311744.277676275
311745	311745.277677986

Even if these two methods are conceptually different, no significant differences can be noticed in the pseudoranges estimates, which are substantially similar, but shifted in time due to the different computation instant.

The solutions obtained using the two different methods appear similar and the variance in the accuracy of the position along the three axes X,Y,Z has the same magnitude in both cases. This fact proves once again that the benefit of using a unique time of reception is especially in speeding up the PVT computation and it is recommended for real time implementations since, while it does not change the receiver accuracy related to the estimate of the user position, it does not require to put any channel in a stand-by state (as told in Section II.B).

Once we stated that the two methods are equivalent, we can evaluate the differences between the results provided by the LS and the EKF algorithms. In the following experiments, we consider both the GPS and the Galileo signals present in the received Signal-In-Space. In Figure 6 we show the 2D estimated trajectory, obtained from a Dataset that simulates a car in motion. The track has been simulated starting from the path obtained using a Novatel receiver tightly coupled with an Inertial Navigation System.

A difference between the solution provided by the LS filter and the smoother one estimated by the EKF can be noticed. As stated before, this improvement is obtained thanks to the adoption of the state-space model and of a system to weight the contribution of the model and of the measurements through the Kalman gain.

In order to better evaluate the differences between the two solutions, we analyse the zoomed area shown in Figure 6. We consider here a portion of straight road, a turning and the same straight road in the opposite direction. It is clear that the LS provides a trajectory which is noisy and is characterized by the presence of some outliers during the turning, making it difficult to clearly identify the path. On the contrary, the Kalman filter provides a smoother trajectory, where the street and the roundabout are clearly visible.

A similar result can be obtained whereas velocity is analysed. The estimated velocities along the three axes are shown in Figure 7.

In this case, the trend of the LS estimates is much noisier than the one obtained running the EKF. However, it can be observed that the estimate provided by the EKF happens to be a smoothed (i.e. filtered) version of the LS estimate.

5. Conclusions

This paper has discussed a receiver architecture that allows to simultaneously process the Galileo and the GPS signals in a software receiver. Despite this topic is known in literature, we focused our attention on some practical implementation details that are often disregarded when the theory is discussed.

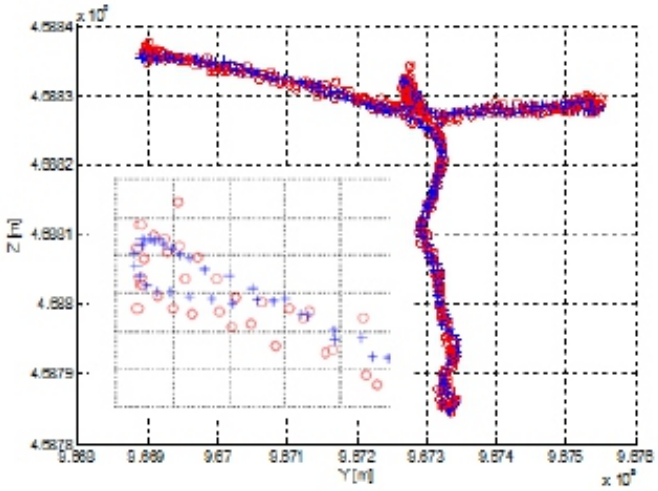

Figure 6. Estimated trajectory, using both a LS (red circles) and an EKF (blue crosses) based receiver, and zoom of the north-western area.

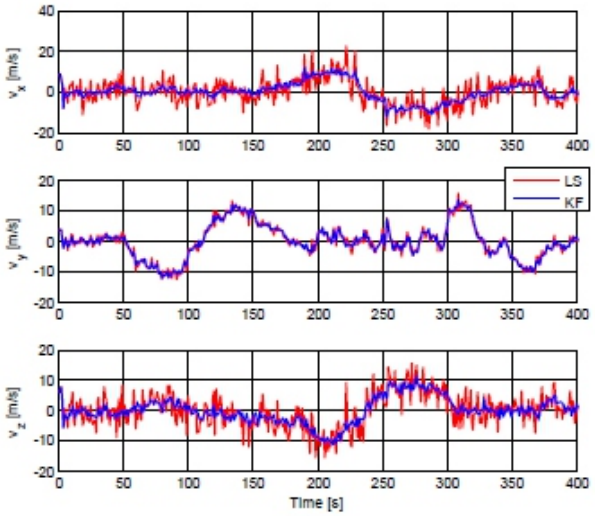

Figure 7. Estimated trajectory, using both a LS and an EKF based receiver, and zoom of the north-western area.

The main effort of this work is towards the implementation of a joint GPS and Galileo receiver, in which particular attention has to be given to pseudorange generation and PVT computation.

At first, we dealt with pseudorange generation, considering two different methods, namely the common transmission time and the common reception time. In the results and in the description, we highlighted why these methods are equivalent from an accuracy point of view, what are their differences and why the common reception time method is more suitable for the integration of the two different satellites systems.

Furthermore, we considered both the LS filter and the EKF, which can be implemented to jointly process GPS and Galileo signals, describing the algorithms and the matrices that must be implemented.

Finally, we provided some comparative results related to the differences between the LS and EKF algorithm, to show why the EKF is nowadays the *de facto* standard when implementing GNSS receivers. Our results show that EKF perform better than a LS-based receiver in the case of both position and velocity estimation.

References

[1] *B. Eissfeller, G. Hein, J.-Á. Ávila-Rodriguez, P. Hartl, S. Wallner, T. Pany, "Envisioning a Future: GNSS System of Systems, Part 1", Inside GNSS, Jan.-Feb. 2007, pp. 58-67*

[2] *"Envisioning a Future: GNSS System of Systems, Part 2", Inside GNSS, Mar.-Apr. 2007. pp. 64-72*

[3] *W.H.W. Tuttlebee, "Software-defined radio: facets of a de- veloping technology," Personal Comm., IEEE , vol.6, no., pp.38-44, Apr 1999*

[4] *J. Mitola, "The software radio architecture," IEEE Comm. Magazine, vol. 33, no. 5, pp. 26–38, May 1995*

[5] *G. MacGougan, P. L. Normark, C. Ståhlberg, "The Software GNSS Receiver," GPS World, Jan. 2005*

[6] *G. Hein, J.-H. Won, and T. Pany, "GNSS software defined radio: real receiver or just a tool for experts?" Inside GNSS, vol. 1, no. 5, 2006*

[7] *M. Fantino, A. Molino, M. Nicola, "N-Gene GNSS Receiver: Benefits of Software Radio in Navigation", in proceedings of the ENC GNSS 2009, May 3-6 2009, Naples, Italy*

[8] *M. S. Braasch and A. J. van Dierendonck, "GPS receiver architectures and measurements,"Proceedings of the IEEE, vol. 87, no. 1, pp. 48–64, 1999*

[9] *G. W. Hein, T. Pany, S. Wallner, J.-H. Won, "Platforms for a Future GNSS Receiver. A Discussion of ASIC, FPGA, and DSP Technologies," Inside GNSS, March 2006, pp. 56-62*

[10] *F.Macchi andM. G. Petovello, "Development of a one chan- nel Galileo L1 software receiver and testing using real data," in Proceedings of the 20th International Technical Meeting of the Satellite Division of the Institute of Navigation (ION GNSS '07), vol. 2, pp. 2256–2269, FortWorth, Tex, USA, 2007*

[11] *M. G. Petovello, C. O'Driscoll, G. Lachapelle, D. Borio and H. Murtaza, "Architecture and Benefits of an Advanced GNSS Software Receiver," Journal of Global Positioning Systems (2008), Vol. 7, No. 2 : pp. 156-168*

[12] *H. Hurskainen, J. Raasakka, T. Ahonen, and J. Nurmi, "Multicore Software-Defined Radio Architecture for GNSS Receiver Signal Processing," EURASIP Journal on Embed- ded Systems, vol. 2009, Article ID 543720, 10 pages, 2009. doi:10.1155/2009/543720*

[13] *M. Sahmoudi and M. G. Amin. 2009. Robust tracking of weak GPS signals in multipath and jamming environ- ments. Signal Process. 89, 7 (July 2009), 1320-1333. doi=10.1016/j.sigpro.2009.01.001*

[14] *M. Zahidul, H. Bhuiyan and E. S. Lohan, "Advanced Multi- path Mitigation Techniques for Satellite-Based Positioning Applications," International Journal of Navigation and Ob- servation, vol. 2010, Article ID 412393, 15 pages, 2010. doi:10.1155/2010/412393*

[15] *F.Macchi, "Development and testing of an L1 combined GPS-Galileo software receiver", PhD Thesis , Department of Geomatics Engineering, University of Calgary, Canada, 2010*

[16] *C.Mongrédien, "GPS L5 Software Receiver Development for High Accuracy Applications", PhD Thesis, Department of Geomatics Engineering, University of Calgary, Canada, 2008*

[17] P.Berglez, "Development of a GPS, Galileo and SBAS re- ceiver", Proceedings of 50th, International Symposium EL-MAR, Zadar, Croatia, 10-12 Sept. 2008

[18] F. Principe, G. Bacci, F. Giannetti, and M. Luise, "Soft- ware-Defined Radio Technologies for GNSS Receivers: A Tutorial Approach to a Simple Design and Implementation," Int. J. of Navigation and Observation, Vol. 2011, Article ID 979815, doi:10.1155/2011/979815

[19] Galileo.ICD,"http://ec.europa.eu/enterprise/policies/satnav/g alileo/open-service/index_en.htm"

[20] GPS.ICD,"http://www.navcen.uscg.gov/pubs/gps/icd200/def ault.htm"

[21] E.D. Kaplan and C.J. Hegarty, "Understanding GPS: prin- ciples and applications", Artec House, 2006

[22] J. Bao and Y. Tsui, "Fundamentals of GPS receivers – 2nd edition", Wiley, 2006

[23] A. Gelb. Applied Optimal Estimation. 1974. Cambridge, MA: MIT Press

[24] M. West and P.J. Harrison, Bayesian Forecasting and Dy- namic Models. Springer-Verlag, New York, 1997 (First edi- tion 1989)

[25] G. Welch, G. Bishop, An introduction to the Kalman filter, SIGGRAPH 2001, Course 8, Los Angeles, CA. Available at: http://www.cs.unc.edu/~tracker/media/pdf/SIGGRAPH2001_CoursePack_08.pdf (accessed: 07.2011)

[26] R.G. Brown and P.Y.C. Hwang, "Introduction to random signals and applied Kalman filtering", John Wiley and Sons, 1997

[27] E. Falletti, M. Rao, S. Savasta, "The Kalman Filter and its Applications in GNSS and INS", in S. A. (Reza) Zekavat, and R. M. Buehrer, Editors, "Handbook of Position Location - Theory, Practice and Advances," in publication by Wi- ley-IEEE Press; Oct. 2011

Facts of Piezo Impedance Technique In Crack Propagation Studies For A Engineering Structure

Dr. Sushil Kumar

A B S T R A C T

In the last two decades, consciousness of structural health monitoring (SHM) has increased many folds especially after witnessing some aerospace/ aircraft failures. Subsequently many SHM techniques have emerged for crack detections. This paper presents one such technique to monitor a crack using piezoelectric transducer (PZT) via electro mechanical impedance (EMI) technique. The basic principle of EMI is to record electro mechanical (EM) admittance signatures resulted from the actuations of PZT (bonded on structure to be monitored) in the presence of electric field. Any deviations in these signatures during the monitoring study indicate disturbance/ damage/ crack (for a healthy structure) or in- crease in severity (if crack/damage is already present). In practice, the occurrence of 'crack' and its 'propagating direction' are equally important. In this paper, basic crack propagation studies on two metallic beam specimens using EMI are presented. Two PZT transducers, one each was bonded on each specimen. First a small crack was induced at different locations on both specimens, it was allowed to propagate in steps (cracks approaching PZT in one specimen and departing in another). Signatures were acquired for un-cracked and cracked propagation stages. Root mean square deviation index was used to demonstrate the experimental observations related to identification of crack propagating directions. Numerical modal analysis was carried out to understand the shifts in modal frequencies during crack propagation. The existence of crack was successfully predicted by EMI but the propagation of crack was not readily obtained. Hence a signature analysis was carried out to predict the propagation direction. It has been a practice to highlight positive sides of any technology, but limitations of EMI are also discussed in this paper and hence the study is expected to be useful for new and existing researchers in the area of EMI based SHM.

Keywords: Monitoring, Damage, Root Mean Square Deviation, Electro mechanical Impedance (EMI), Crack, Steel, Propagation

1. Introduction

Consciousness of structural health monitoring (SHM) of either metals or non metals has increased many folds in the recent times. Subsequently many SHM techniques have emerged to monitor the condition of structure to find out crack / instability at earlier stage of occurrence. The most common SHM techniques are visual inspection, low frequency vibration techniques, statistical structural response techniques, localized non destructive evaluation (NDE) techniques.

However, the recent advent of smart materials based sensors has given rise to new classification of

SHM i.e smart materials based monitoring techniques. There are many smart sensors like fiber optics (FOS), polyvinylidene fluoride (PVDF), micro fiber composites (MFCs), piezo-electric polymers and ceramics, electro-rheological (ER) fluids, magnetostrictive materials and shape memory alloys (SMA). But the piezoceramic transducers (PZTs) and MFCs, which are 'sensors and actuators' are accepted as key contributors in noise and vibration control[1- 3]. Its application in electromechanical impedance (EMI) tech-nique[4] is also accepted as one of the latest monitoring tool for engineering structures[5-10]. In the EMI technique, the PZT or MFC transducer is either surface bonded on or embedded inside the host structure. The governing principle is that the transducer actuates harmonically in the presence of electric field to produce a structural response, which is known as electromechanical (EM) 'admittance signature'. The EM admittance signature is a function of the stiffness, mass, damping of the host structure[4], the length, width, thickness, orientation[11], mass[12–13] of the transducer, and the adhesive[14]. The 'changes' in the EM 'admittance signature', which is the inverse measure of mechanical impedance of the structure are indicative of the presence of structural 'damage'. In the past decade, many researchers have developed EMI models to describe the interaction between the transducer and the host structure for SHM. Sub-sequently many experimental studies were conducted to verify these models. This present study provides one such study were the experiments were compared with numerical and statistical based methods. The objective addressed in this paper is to monitor progressive crack (on surface of metallic beam specimens) such that the dimension of the crack increases in steps.

Two PZT transducers, one each on a beam were bonded at one end on the surface using epoxy adhesive. These transducers were connected to impedance analyzer. First a small crack was induced at different locations on both beams, it was allowed to propagate in steps (cracks approaching PZT on one beam and departing on another). Signatures were acquired throughout the monitoring period (for increasing severity of crack); say if 10 signatures were obtained for 10 stages of crack severity increments, they were compared with all its preceding stage signatures. That is, 10th signature is compared with 1 to 9 signatures, 9th is compared with 1 to 8 and so on. Numerical modal analysis for crack propagation was carried out to understand the shifts in modal frequencies. Additionally, statistical based root mean square deviation (RMSD) index was used to demonstrate the crack propagation direction. Furthermore facts related to this investigation were clearly presented.

2. Background of EMI Technique

In general, the actuation mechanism[15] of the PZTs in the presence of electric fields can be divided into extensional (along X and Y directions), longitudinal (along Z direction) and shear actuations

(along XZ and YZ planes). Where E_1, E_2 and E_3 represent the electric fields along X, Y and Z directions as shown in Figure 1. The PZT in the presence of E_1 and E_2 produces shear actuations (d_{33}, d_{24}), and in the presence of E_3 produces extensional actuations (d_{31}, d_{32}) and longitudinal actuation (d_{33}). Note that d_{3j} is the strain displacement coefficient, related to the normal strains in the presence of E_3, and the subscript j denotes either the X, Y or Z direction. d_{15} and d_{24} are the strain displacement coefficients related to shear strains in the XZ and YZ planes developed due to the fields E_1 and E_2 respectively. However for EMI techniques, only electric field E_3 is applied along Z direction, thus the PZT produces only extensional and longitudinal actuations.

As a result of these, the vibrations along the length, width and thickness of the PZT are produced[7]. Thus, when PZT is surface bonded on or embedded inside any host structure results in these actuations. The actuations imparted on the structure are forced vibrations. However, the structure tries to resist these vibrations resulting in a reaction to applied force. As stated earlier, PZT is both actuator and sensor. Hence it measures the inverse of this reaction force of the structure interms of its admittance which is inverse of im-pedance (is a ratio of reaction force over the velocity output). The admittance ($\bar{Y}_c$) is a complex term, and can be divided into real (conductance) and imaginary (susceptance) parts as given below

$$\bar{Y}_c = G + Bj \qquad (1)$$

Where G and B are the conductance and susceptance respectively.

The conductance signature has been used mostly in damage or crack[4, 6, 8, 16] or axial load/ stress[17, 18] monitoring of metals, while the susceptance has been used for delaminating studies of composites, bonding layers and transverse load monitoring[19] on metals. Hence in the present study conductance signatures were considered as the specimens were subjected to crack propagations.

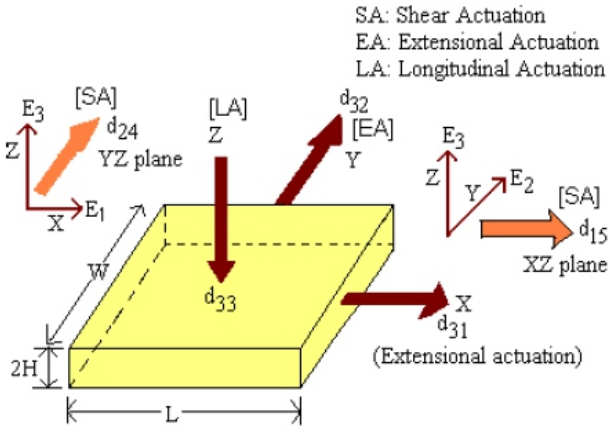

Figure 1. Actuations of PZT

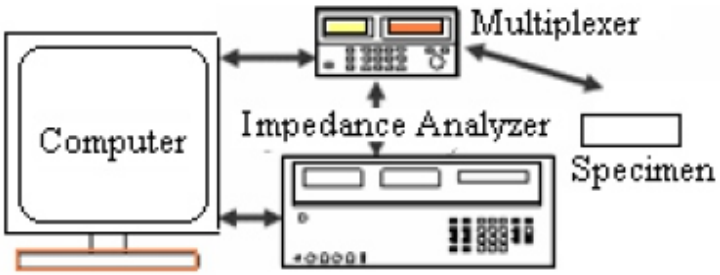

Figure 2. Schematic diagram of the experimental setup

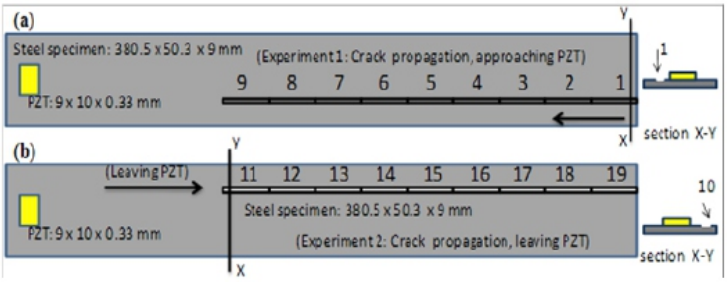

Figure 3. Specimens (a) crack approaching PZT (b) crack leaving PZT

3. Experimental Investigations

3.1. Experimental Setup

The experimental setup (Figure 2) used for acquiring ad-mittance signatures consisted of a Hewlett Packard 4192A impedance analyzer, a 3499A/B switching box (multiplexer), specimens and a personal computer. Two identical beams, made of metal alloy (Table 1) of dimensions 380.5 x 50.3 x 9 mm were used as the specimens in this study. Two identical PZTs of dimension 9 x 10 x 0.35 mm were surface bonded on these specimens at 10.5 mm away from one of the edges as shown in Figure 3. PZTs were wired to the impedance analyzer through the switch box, and actuated with a sinusoidal 1V RMS electric supply. The experimental EM admittance signatures i.e conductances were then acquired for the desired frequency ranges. Thus, the specimens through the PZTs, are connected to the analyzer via the multiplexer. These PZTs diagnose the crack propagation on the surface of specimens.

The properties of the specimens, PZTs and the epoxy adhesive used to bond these PZTs on the beams are listed in Table 1. Beams rested freely on a foam bed and a ‘free-free’ boundary condition was assumed to prevail in the experimental study. Two experiments (Experiment 1 and Experiment 2) were conducted with the specimen as follows.

Table 1. Key properties of epoxy, metal alloy and PZT

Physical property	**Values**		
Mechanical	**Epoxy**	**Metal Alloy**	**PZT**
Density (kg / m^3)	1180	2715	7800
Young's Modulus (N / m2)x 109	2	68.95	66.67
Poisson ratio, υ	0.4	0.33	0.3
Loss factor, η	-	-	0.023
Electrical			**PZT**
Piezoelectric strain coeff. $d31$, $d32$ (m/V) x 10^{-10}			-2.1
Piezoelectric strain coefficient d_{33} (m/V) x 10^{-10}			4.5
Dielectric loss factor, δ			0.015
Electric permittivity, ε_{33} (farad/m) x 10^{-8}			1.75

Experiment 1: An initial (baseline) signature of the PZT bonded on first beam specimen was obtained from imped- ance analyzer for the frequency range of 0-500 KHz (a wide range as recommended by Park et al[16] was considered). Let the signature be designated as 'S0'. A crack of dimension 20 mm x 2 mm x 1 mm (say crack 1) was induced on the right edge on surface of the beam and a signature was recorded again; say it is designated as S1. Later, eight more cracks of same dimensions were induced one after the other on surface of the beam such that the crack propagated from far end towards PZT along length direction as shown in Figure 3(a). After inducing each crack, signature was recorded. Thus, a total of ten signatures were obtained for no crack (i.e S0), 20 mm (for crack 1, i.e S1), 40 mm (cracks 1 & 2, i.e S2), 60 mm (cracks 1, 2 & 3, i.e S3) and so on as shown in figure. They were designated from S0-S9 respectively.

Experiment 2: An initial (baseline) signature of the PZT bonded on second beam specimen was obtained from im- pedance analyzer for the frequency range of 0-500 KHz as similar to experiment 1. Let the signature be designated as 'S10'. A crack (of same dimension as made before) was induced 170 mm away from the PZT along length direction (at about centre of beam) on the specimen (say crack 11). Followed by eight more cracks, induced one after the other which propagated away from the PZT i.e from centre to far end (opposite direction as compared to crack propagation on first specimen) as shown in Figure 3(b). At every cracked stage, signatures were acquired and were designated from S11-S19 respectively.

Figure 4 shows the signatures of all crack propagation stages for experiments 1 and 2 in the considered frequency range of 0- 500 KHz. Both the figures show that the intensities of the signature are similar with similar peaks and valleys.

The objective in this study is to identify the crack propagating directions using the signatures. However, it is hard from the figure to identify any difference between the two experiments. Hence in the next section, statistical based RMSD index was introduced to estimate the amount of deviation of signatures.

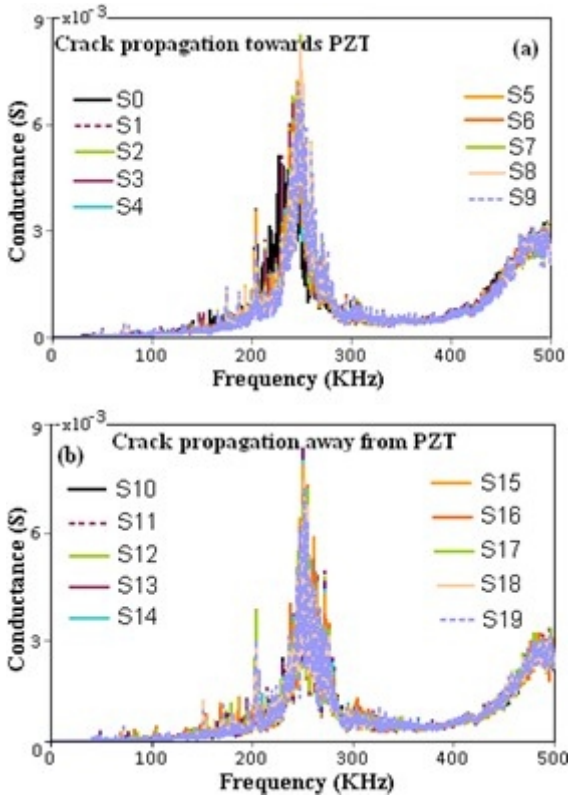

Figure 4. Signatures of all stages (a) experiment 1 (b) experiment 2

4. Statistical Investigations

Root Mean Square Deviation (RMSD) Index

There are few pattern recognition techniques such as 'signature assurance criteria' and 'adaptive template matching' to quantify changes in acceleration signatures[20] in addition to the RMSD indices[21-24] for comparisons between signatures of two different states. RMSD has been widely accepted and used for estimation of amount of variation between any two signatures. It is defined as

$$RMSD^k\ (\%) = \sqrt{\frac{\sum_{i=1}^{N}\left(y_i^k - x_i\right)^2}{\sum_{i=1}^{N} x_i^2}} \times 100 \qquad (1)$$

where χ_i and y_i^k (i = 1,2,3…N) are signatures obtained from the PZT bonded to the structure before and after the damage (k^{th}) is incurred, respectively. Where i=1, 2, 3...N indicates the frequencies where the value of admittance was collected. The RMSD is a comparable index of initial sig-nature (χ_i) with later stage signatures y_i^k (k = 1, 2,3 …). In the present study the RMSD index was adopted to evaluate the conductance signatures obtained from the 'PZT-specimen' system. For this purpose, two types of RMSD values were evaluated for each crack magnitude. The first one (type -1) was the deviation of the signature of a particular cracked state (say S1 and S11 for experiments 1 and 2, respectively) with respect to (w.r.t) the baseline signature (S0 and S10 for experiments 1 and 2, respectively). The second (type-2) was the quantitative deviation of the signature w.r.t the signature of the immediate state (i.e the deviations of signatures S2 to S9 w.r.t S1; S3 to S9 w.r.t S2; S4 to S9 w.r.t S3 and so on). The type-2 can be termed as 'subsequent-state-index'. If y_i^{k-1} and y_i^k are the signatures obtained for the state of the specimen at $(k\text{-}1)^{th}$ and k^{th} crack magnitudes, respectively, then the subse-quent-state-index for the state at k^{th} crack magnitude is given by replacing x_i by y_i^{k-1} in Equation 1.

Tables 2 and 3 list the quantitative deviations of signatures (S1 to S9) w.r.t S0 (no crack), i.e type 1 RMSD for experiment 1, and deviations of signatures (S11 to S19) w.r.t S10 (no crack) for experiment 2. From the tables, it can be seen that as the crack severity or propagation length increases, the RMSD value increases for both the experiments. From Figure 4 and Tables 2-3, it is understood that EMI method is effective in predicting the severity of damage but the propagation direction could not be established. Thus this is one limitation of EMI technique.

From careful examination of Figure 4, it was observed that there is lack of repeatability of signatures. If both specimens are identical, baseline signatures of both specimens, S0 and S10 should be identical. However, small deviations in magnitudes of signatures were observed (which may not be obvious from figure), which implies that even though the two specimens are identical, the baseline signatures (S0 for experiment 1 and S10 for experiment 2) are not the same and hence the PZT did not yield identical signatures. This is because of many reasons for example the specimens may not be 'exactly' identical or the bonding positions of PZT may not be 'exactly' identical on the beams resulting in variations of baseline signatures. Thus, it can be stated that EMI tech-nique will not yield unique signatures even if there is slight variations in bonding positions of transducer or if specimen is not exactly identical. Thus,

the transducer is very sensitive and subsequently, it may not be possible to replicate (produce same) signatures in practical cases were structures are larger /complicated than the experiments undertaken in the present study.

In general, if crack is near the PZT i.e say S11 (crack 20 mm), the statistical deviation (RMSD) w.r.t signature S10 (no crack, experiment 2) should be more than RMSD of crack, far from the PZT i.e S1 (crack 20mm) w.r.t signature S0 (no crack, experiment 1). But the obtained RMSD values are respectively 5.58 % and 26.6 %, which is in contrast. This is another limitation of EMI technique.

Tables 2 and 3 shows that as the crack severity increases, the RMSD values also increases indicating that PZT is relatively smarter in assessing the severity of the crack for a considered specimen if the PZT location does not alters throughout the experimental period. To further study the behaviour, type 2 RMSD study was carried-out as given in Tables 4 and 5 for experiments 1 and 2, respectively.

One more drawback in this EMI technique is that the crack propagation directions (with respect to PZT) in both cases of experiments are opposite but still the Type 1 RMSD values show similar increments as crack severity increases (Tables 2-3). Type 2 RMSD yielded decreasing values as we go towards right (increasing severity) as given in Tables 4 and 5 for both experiments. Again, it is difficult to differentiate the propagation direction. Thus, even this statistical investigation (types 1-2) also failed to understand the propagation direction even though it was able to predict the severity of crack. So, numerical study was carried-out as shown in next section to check if at least this can give any further information about crack propagation direction.

Table 2. Type 1 RMSD values for Experiment 1

Signature	S1	S2	S3	S4	S5
RMSD	26.6	29.65	32.57	33.56	34.43
Signature	S6	S7	S8	S9	
RMSD	41.15	42.54	43.41	43.42	

Table 3. Type 1 RMSD Values for Experiment 2

Signature	S11	S12	S13	S14	S15
RMSD	5.58	6.79	13.75	18.7	22.35
Signature	S16	S17	S18	S19	
RMSD	27.82	30.01	30.89	33.43	

Table 4. RMSD Variations for crack propagating towards PZT

Signature	w.r.t							
	S1	S2	S3	S4	S5	S6	S7	S8
S1	0							
S2	5	0						
S3	8.35	5.83	0					
S4	15.5	15.6	12.8	0				
S5	16.2	16	13	3.6	0			
S6	20.3	17	13.3	16	14.9	0		
S7	22.4	19.4	15.8	17.2	15.8	4.6	0	
S8	23.6	20.2	16.9	19.3	17.9	5.5	3.5	0
S9	25.3	22.7	19.7	19.2	17.9	11	9	8.7

Table 5. RMSD Variations for crack propagating away from PZT

Signature	w.r.t							
	S11	S12	S13	S14	S15	S16	S17	S18
S11	0							
S12	6.5	0						
S13	15.2	10.9	0					
S14	20.3	16.5	7.8	0				
S15	23.9	20.5	13.5	7.8	0			
S16	29	26.8	24	20.7	16.8	0		
S17	31	29.2	27.3	25	22.2	11.6	0	
S18	31.4	30.3	29.4	27.8	25.5	18.5	11.9	0
S19	33.8	32.8	32.4	31	28.9	22.7	15.6	9.9

5. Numerical Investigation

A numerical modal analysis was carried out using ANSYS[25] for both identical specimens. In the modal analysis (with appropriate meshing size) four types of mode shapes namely, axial, flexural, movement in XZ and twisting in XYZ space were observed, where X, Y and Z represent directions along length, width and thickness of the beam.

For both types of crack propagations, the shifts in modal frequencies (of first 20) were found to be similar and thus it was difficult to find out the propagation direction even in numerical investigation. Figure 5 shows the modelling and model frequency distribution graphs of two types of crack

propagations (i.e for experiment 1 and 2). There exists no difference between Figures 5 (c) and (d). The modal frequencies of first twenty mode shapes of the experiment 1 are listed in Tables 6 and 7. The model frequencies for experiment 2 are similar to experiment 1.

6. Merits & Demerits of EMI Technique

The (1) experimental study, the (2) RMSD indices and the modal analysis have not been able to predict the direction of crack propagation. i.e., no trends were observed in the (1) experimental signatures and (3) modal analysis, where as 'increasing trends' of (2) RMSD were observed for both directions of crack propagation (towards and away from PZT), this questions the applicability of EMI to study crack propagation using wide range of excitation frequency even though the RMSD increases as magnitude of crack increases.

Table 6. Modal frequencies in HZ as crack propagates towards PZT (part a)

Modes	No crack	Crack 1	Cracks 1, 2	Cracks 1,2,3	Cracks 1,2,3,4	Cracks 1,2,3,4,5
1	897.52	896.82	899.02	897.23	896.33	896.41
2	1046.6	1049.3	1041.7	1044.1	1051.3	1057.8
3	1378.1	1374.8	1379.3	1374.3	1372.2	1372
4	1652.8	1657.2	1661.6	1655.2	1652.6	1659.7
5	2508	2510.5	2487.9	2495.2	2491.3	2480
6	2955	2962	2965.6	2948.6	2962.3	2956.7
7	3588.2	3609.5	3583.8	3583.1	3552	3582.4
8	4492.1	4517.8	4512.9	4516.8	4486.6	4505.3
9	5057.7	5059	5068.5	5047.7	5057.6	5059.1
10	5708.4	5751.1	5658.3	5662.2	5627	5721.6
11	6569.1	6639.3	6625.9	6581.2	6558.1	6643.6
12	6831.7	6835.8	6828.5	6829	6826.1	6833.1
13	7591.2	7596.7	7541.4	7536.7	7462.1	7554.5
14	8159.5	8168.2	8144.8	8139.9	8128.8	8145.3
15	8957.5	9004.9	8915.5	8874.5	8889.7	8921.1
16	10012	10088	10015	9970.3	9959.3	10045
17	11844	11864	11841	11750	11738	11809
18	11894	11945	11934	11885	11890	11904
19	12581	12679	12556	12545	12553	12639
20	13365	13370	13365	13365	13362	13363

Table 7. Modal frequencies in HZ as crack propagates towards (part b)

Modes	Cracks 1,2,3,4,5,6	Crack s1,2,3,4,5,6,7	Cracks 1,2,3,4,5,6,7,8	Cracks 1,2,3, 4,5,6,7,8,9
1	898.55	896.96	899.11	897.72
2	1045.5	1037.3	1050.8	1047.9
3	1371.5	1372.3	1374	1371.3
4	1649.3	1645.4	1657.3	1654.4
5	2488	2453.3	2528.3	2513.2
6	2943.4	2960	2943	2942.4
7	3581.4	3547.6	3596.6	3586.6
8	4527.6	4500	4552.8	4489
9	5046.5	5055.2	5046.5	5042.3
10	5714.8	5592.8	5707.9	5706.1
11	6635.4	6594.5	6693.5	6625.6
12	6833.1	6822.4	6833.5	6827.6
13	7576.6	7462.5	7619.3	7593.7
14	8151.2	8138.1	8141.8	8159.1
15	8958.2	8898	9049.6	8984.7
16	10010	9922.8	10100	10043
17	11841	11774	11857	11841
18	11868	11883	12002	11920
19	12588	12435	12608	12636
20	13360	13353	13359	13362

In practice, the occurrence of 'crack' and its 'propagating directions' are equally important. In general, if there are any changes in structure either in the form of stiffness variations, increase / decrease in load magnitude or occurrence of crack. There exist some changes in EM signatures in the form of peak/valley, as they shift either to right or left; decrease or increase in magnitude. Thus it can be stated that the main advantage of EMI technique is to predict disintegrity/crack/load/damage presence on structure to be monitored and its severity.

This investigation presents the following limitations and advantages of using EMI technique for crack propagation study.

The main limitations of EMI are

1. EM admittance Signatures (Figure 4) in the range of 0-500 KHZ, suggest that as the crack magnitude increases, there existed shifts in the peaks and valleys for both experiments. But there is no pattern of shifts; hence propagation of crack direction cannot be predicted.

2. Statistical RMSD values show that (Tables 2 to 5) as the crack magnitude increases, similar changes in values occur for both experiments thus making it difficult to predict crack propagation direction.

3. Numerical model analysis for both experiments yielded similar results (Figure 5). Thus crack propagation direction cannot be found out.

However, there exist few merits of EMI technique as follows

1. Presence of crack on any specimen can be predicted

2. Increase in severity of crack can be predicted (RMSD values increased as severity of crack increased).

Further, to identify the difference between crack propagation directions a small search was carried out in the signatures (Figure 4) as follows.

6.1. Signature Analysis

A closer study of peaks and valley of the signatures of Figure 4 was carried out (as shown in Figure 6). That is, in Figure 4(a-b) a peak was found at frequency range of 23-24 KHz, which resulted in decrease in signature magnitude as the crack propagated towards, and increases as crack propagated away from PZT.

So it is possible to predict the propagation direction by inspection of peaks and valleys, which is another advantage of EMI technique. However, the search was random and hence it cannot be generalized. The frequency range of 23-24 KHz is so narrow to be considered as logically correct.

However the present study indicates that EMI technique is still in the infant stage without many practical applications[26], even though it has potential and sensitivity for prediction of cracks etc.

So, future studies are compulsory to implement EMI technique in SHM applications for real practice. Hence future research should concentrate on narrow frequency range studies (example: 50- 100 KHZ, 100-150 KHZ and so on) within a wide range of frequency band to understand various issues like (a) multiple cracks, (b) axial loading pattern and (c) transverse loading patterns (d) fatigue etc on structures to be monitored. In addition to this, the electric supply to the transducer in practical applications is difficult[26] as there can be multiple PZT transducers with several electric supply wires. Hence a way of energy harvesting to the PZT transducers[27, 28] should be considered. Thus there are several factors which should be considered before considering EMI techniques to actual practice[26].

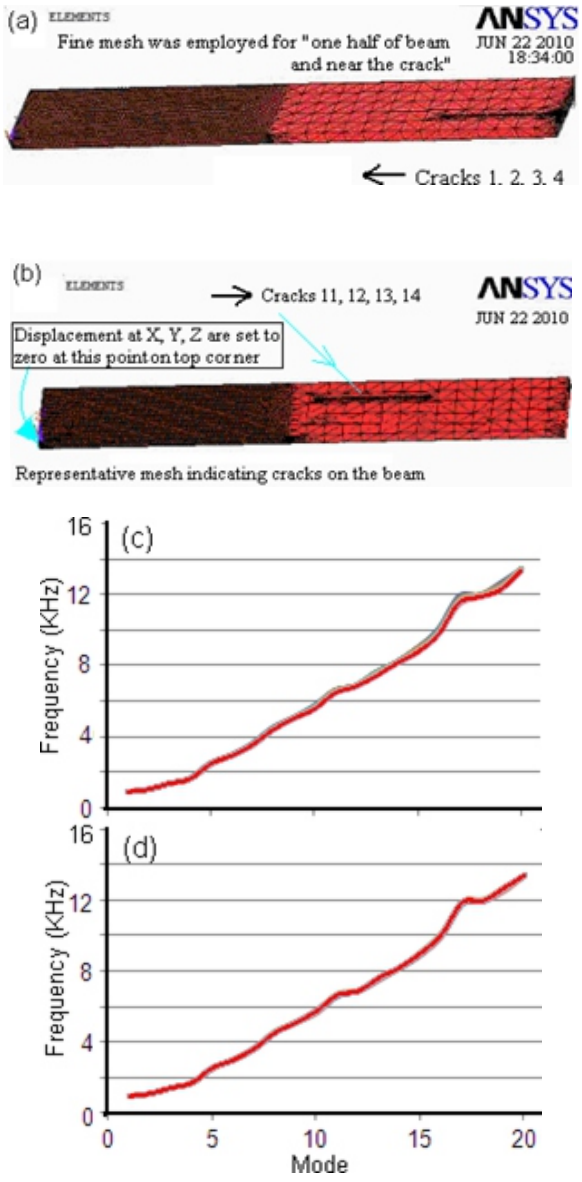

Figure 5. Modelling and model frequency distribution graphs (a) Representative meshing of 4 cracks (b) Frequency distribution graph for all cracks propagating towards left (c) Representative meshing (d) Frequency distribution graph for all cracks propagating towards right

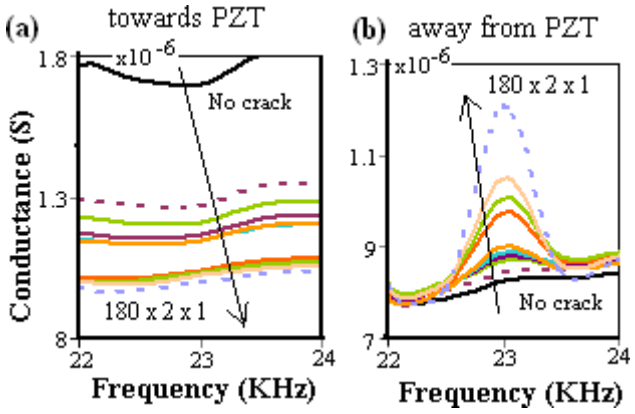

Figure 6. Conductance signatures (a) Experiment 1 (2) Experiment 2

7. Conclusions

Consciousness of SHM of either metals or non metals has increased many folds in the recent couple of decades. Subsequently many SHM techniques have emerged to monitor the condition of structure to find out damage/ instability at earlier stage of occurrence. However, the EMI technique which is a recently developed classification of SHM can provide a promising monitoring solution for many engineering structures if its limitations as presented in this study are addressed. Detection of any crack, generated in the sensing zone of PZT at earlier state of its occurrence using EMI technique is possible. Even its magnitude can be predicted but its direction of propagation cannot be predicted with logic (however a signature analysis can be carried out into the narrow frequency ranges to predict the direction of crack propagation). This paper presented a study of progressive crack i.e crack propagation towards and away from PZT. RMSD index was found to increase continuously for the considered frequency range as crack magnitude increased in both experiments. However, in practice, the occurrence of 'crack' and its 'propagating directions' are equally important. In this study, the crack propagation direction was not properly predicted even though 'peak study of signatures' i.e signature analysis had shown that the frequency range of 22 to 24 KHz was able to clearly differentiate two directions of crack propagations. But the fact is that the frequency range is too narrow, and the search to find this range was random. Hence future studies should continue to improve EMI technology for crack propagation studies and practical applications. This paper is expected to be useful for new researchers planning to work in the area of EMI technique as the experiments presented here are very basic and important. This paper also clearly presents that the existing researchers in this area should concentrate on addressing issues like multiple crack detection etc before actually applying in practice.

References

[1] Boller C. 2002. "Structural Health Management of Ageing Aircraft and Other Infrastructure", Monograph on Structural Health Monitoring, Institute of Smart Structures and Systems (ISSS), pp. 1-59, 2002.

[2] Rao, K, N., Bhat, M, S., and Ganguli, R., "Experimental Demonstration of H-alpha Control based Active Vibration Suppression in Composite Fin-tip of Aircraft using Optimally Placed Piezoelectric Patch Actuators", Journal of intelligent materials systems, Vol.19, pp. 651-669, 2000.

[3] Kumar, D. N, Raja. S and Ikeda T.," Active vibration control of smart plates with partially debonded multilayered PZT actuators", Smart Materials and Structures Vol. 16 no. 5 , pp.1584, 2007

[4] Sun, F. P., Chaudry, Z., Rogers, C. A., Majmundar, M., and Liang, C.,. "Automated real-time structure health monitoring via signature pattern recognition", Proceedings of the Smart Structures Materials Conference, San Diego, California, Feb. 27- Mar. 1, Proc. SPIE, Vol. 2443, pp. 236-247, 1995.

[5] Park, G, Cudney, H. H. and Inman, D. J. "Impedance-based health monitoring of civil structural components, Journal of Infrastructure System, ASCE Volume 6, pp.153–60, 2000.

[6] Ritdumrongkul S, Abe M, Fujino Y and Miyashita T. "Quantitative health monitoring of Bolted joints using a piezoceramic actuator sensor", Smart Materials and Struc- tures, Volume 13, pp. 20–9, 2004

[7] Annamdas, V. G. M, and Soh, C. K, "Three-Dimensional Electromechanical Impedance Model. I: Formulation of Directional Sum Impedance", Journal of Aerospace Eng., Vol 20, no.1, pp. 53-62, 2007.

[8] Annamdas V. G. M and Soh C. K "Application of Electromechanical impedance technique for Engineering Structures: Review and Future Issues", Journal of intelligent material systems and structures Vol 21, no.1, pp. 41-59, 2010.

[9] Zhao X, Gao H, Zhang G, Ayhan B, Yan F, Kwan C and Rose J L. "Active health monitoring of an aircraft wing with embedded piezoelectric sensor/actuator network: I. Defect detection, localization and growth monitoring", Smart Materials and Structures, vol. 16, no. 4, pp. 1218-1225, 2007.

[10] Annamdas V. G. M, Yang Y and Soh C. K "Impedance based Concrete Monitoring using Embedded PZT Sensors" International Journal of Civil & Structural Engineering, Vol 1, no. 3, PP: 414-424, 2010.

[11] Wetherhold, R., Messer, M., and Patra, A., "Optimization of directionally attached piezoelectric actuators", Journal of Engineering Materials and Technology, vol.125, no.2, pp:148-152, 2003.

[12] Madhav, A. V. G and Soh, C. K. "Multiplexing and uniplexing of PZT transducers for structural health monitoring". Journal of Intelligent Material systems and structures, vol. 19, no. 4, pp. 457-467, 2008.

[13] Cheng, C. C.; Lin, C. C. "An impedance approach for determining optimal locations and shapes of multiple induced strain actuators", Smart Materials and Structures, Vol.14, pp.1120-1126, 2005.

[14] Madhav, A. V. G and Soh, C. K "Electromechanical Impedance Model of Piezoceramic Transducer - Structure in Presence of Thick Adhesive Bonding", Smart Materials and Structures, vo.16, no.3, pp. 673-686, 2007.

[15] *Raja, S. Sreedeep, R., and Prathap, G. "Bending behavior of Hybrid- Piezoelectric Sandwich Beams", Journal of Intelli- gent Material Systems and Structures, vol. 15, no. 4, pp. 611-619, 2004.*

[16] *Park, G., Sohn, H., Farrar, C. R. and Inman, D. J. "Overview of Piezoelectric Impedance-Based Health Monitoring and Path Forward", The Shock and Vibration Digest, SAGEPublications, Vol. 35, no.6, pp. 451-463, 2003*

[17] *Ong, C. W., Yang, Y. W, Naidu, A. S. K., Lu, Y and Soh, C. K,. "Application of the electro-mechanical impedance method for the identification of in-situ stress in structures", Smart Structures, Devices, and Systems, Proceedings of SPIE (16-18 Dec., Melbourne, Australia), volume 4935, pp. 503-514, 2002.*

[18] *Ab´e M, Park G and Inman D J "Impedance-based monitoring of stress in thin structural members", Proceedings of. 11th Int. Conference on Adaptive Structures and Technologies (Nagoya, Oct.): pp. 285–92, 2000.*

[19] *Annamdas, V. G. M, Yang Y and Soh, C. K. "Influence of loading on the electromechanical admittance of piezoceramic transducers", Smart Materials and Structures, vol.16, no.5, pp.1888-1897, 2007.*

[20] *Samman, M. M. and Biswas, M."Vibration Testing for Non-Destructive Evaluation of Bridges II: Experiment', Journal of Structural Engineering, ASCE, vol. 120, no. 1, pp 290-306, 1994.*

[21] *Giurgiutiu, V. and Rogers, C. A.. "Recent Advancements in the Electro-Mechanical (E/M) Impedance Method for Structural Health Monitoring and NDE", Proceedings of Smart Structures and Materials Conference, San Diego, California, March, SPIE Volume 3329, pp. 536-547, 1998.*

[22] *Naidu A S K and Soh C K "Identifying damage location with admittance signatures of smart piezo-transducers", Journal of*

Intelligent Material Systems and Structure, vol. 15, pp. 627–642, 2004

[23] *Park, S., Ahmad, S., Yun, C. B., and Roh, Y.. "Multiple Crack Detection of Concrete Structures Using Impedance-based Structural Health Monitoring Techniques", Experimental Mechanics, vol. 46, no.5, pp. 609-618, 2006.*

[24] *Yang Y, Hu Y and Lu Y. "Sensitivity of PZT Impedance Sensors for Damage Detection of Concrete Structures", Sensors, vol.8, pp. 327-346, 2008.*

[25] *ANSYS ANSYS Reference Manual: Release 8.0, ANSYS Inc., Canonsburg, PA, USA,2010.*

[26] *Annamdas, V. G. M. and Yang, Y., "Practical implementation of piezo-impedance sensors in monitoring of excavation support structures. Structural Control and Health Monitoring, 19: 231–245 (doi: 10.1002/stc.418), 2012*

[27] *Sodano, H. A., Inman, D. J., and Park, G. "A Review of Power Harvesting from Vibration using Piezoelectric Materials", The Shock and Vibration Digest Vol. 36, pp. 197-205, 2004*

[28] *Ericka, M., Vasic, D., Costa, F., Poulin, G., and Tliba, S. "Energy harvesting from vibration using a piezoelectric membrane", Journal De Physique Iv, Vol. 128, pp. 187-193, 2005*

Investigation of Active Flow Control Over Naca0015 Airfoil Via Blowing

Mr. Mina Negi

A B S T R A C T

In this study the concept of Active flow control using a blowing jet with a width of 2.5% of chord length which places on NACA0015 airfoil's upper surface under Re=455000 in 6 different angles of attack 12° to 17° is investigated. More than 200 numerical simulations are conducted over a range of parameters of jet locations (10%, 30% and 50% of chord from leading edge), jet velocity ratios (1, 2 and 6 time of free stream velocity) and jet angles (0°, 30° and 45°relative to the airfoil surface) are investigated. The viscous model used for modeling the turbulence is Spalart-Allmaras and a commercial CFD code, the FLUENT, is used to solve flow equations. Simulation results show that the blowing will increase the amount of lift and reduce drag. Also at high angles of attack, the blowing delay separation and improve the performance of the airfoil.

Keywords: Flow Control, Blowing, NACA0015, CFD

1. Introduction

Man has never been satisfied with the world that surrounds him, and tried to control or improves it from the very beginning to get more beneficial effects. This applies to almost all science disciplines nowadays, and fluid Mechanics is not an exception. Since early times, fluid was an attractive and at the same time difficult to understand subject that forced investigators to improve their skills and knowledge. Even after understanding some of the complicated fluid behaviour investigators were never satisfied, and put also their efforts on controlling it. That's where the discipline of Flow Control was born.

The benefit of modern flow control techniques common to all of the areas is the ability to achieve large-scale changes in flow behaviour with low levels of energy input. This implies that some amplifying mechanism exists in the flow which the actuator triggers, enhances or suppresses in some way[1].

Flow control provides the enabling technology for many of the advanced vehicles. Both passive and active technologies can play an important role. When changing flow conditions are not the critical issue, passive technologies offer the promise of simplicity. Active flow control enables optimization at off design conditions or when it becomes necessary to react to rapidly changing flow conditions[2].

The benefits of flow control have become more importantas the nature of aircraft changes. With the advent of stealth the need for a method of control with fixed surfaces has grown. Also, economic interests have demanded more weight savings in the interest of fuel economy. This demand has lead to the demand for increased lift-to-drag ratios. Synthetic jets have made it possible to protect an aircraft from flow separation thus staving off the undesirable effects of stall. Stall leads to loss in lift and a tremendous increase in drag forces[3].During take-off and landing, the wings of airplanes have to generate an enormous amount of lift at low flight velocity. In modern commercial aircraft, this is realized by complex multi-element high-lift devices. As these cause additional weight, increased constructive effort, etc., there exists a significant economical interest in replacing the multi-element devices by single flaps. However, such flaps are only applicable if flow separation at high flap angles can be controlled. One possibility for active separation control is suction and/or blowing. Most applications incorporate excitation at the leading edge in order to affect the boundary layer upstream of the point of separation, with steady or periodic suction and blowing[4].By preventing separation, lift is enhanced and form drag is reduced. Suction and blowing of primary fluid can have significant effects on the flow field, influencing particularly the shape of the velocity profile near the wall and thus the boundary layer susceptibility to transition and separation[5].

The first use of a steady air jet for lift enhancement in the United States was reported by Knight and Bamber (1929). Their experiments investigated the effect of the jet slot width, slot location, and air supply pressure inside the airfoil (which dictated the jet flow rate) on the increment in lift. They demonstrated a 151% increase in L/D for a conventional two-dimensionalairfoil[6].

The momentum coefficient, first defined by Poisson-Quinton (1948) as

$$C_{\mu} = \frac{q_m v_j}{q_0 S} \qquad (1)$$

was found to be an effective scaling parameter for the dependence of the lift increment on the amplitude of jetblowing actuators. In this definition q_m and v_j are the mass flow rate and velocity of the actuator jet, respectively, while $q_0 = 1/2\,\rho v^2$ is the dynamic pressure and S is the planform area[7].

An extensive review of BLC research up to 1960 can be found in the two-volume monograph edited by Lachmann (1961)[8] and more recent by Mohammad Gad-el-Hak up to 2000[9].

A large body of fundamental research used open-loop forcing to study optimum forcing frequencies and minimum forcing amplitudes necessary to maintain an attached flow, or to reattach a separated flow

over a flap or an airfoil. Some early fundamental work was by Katz et al. (1989)[10], and an extensive review of open-loop separation control has been given by Greenblatt and Wygnanski (2000)[11].

Control of flow separation and transition point by means of different mechanisms such as using leading edge devices, blowing, and suction have been quite extensively researched. Wong et al.[12]investigated control effects on a NACA 0012 airfoil with a spanwise blowing located at 0, 25 and 100% from the leading edge at the angle of attack from -20° to 20°. Huang et al.[13]studied numerically control effects on a NACA0012 airfoil with a jet (2.5% width) located at various locations and jet angle and amplitude at the angle of attack of 18°. Schatz and Thiele[14]studied a two element high lift configuration at stall condition by a numerical simulation based on RANS method and flow separation delayed by periodic vertical suction and blowing through a slot close to the leading edge of the flap.

All of the above studies find that the synthetic jet and forcing/non-forcing (oscillatory/steady) suction/blowing on the aerofoil leading edge can increase lift and decrease drag. Many other experimental work (Seifert and Wygnanski[15], Tinapp[16], WU[17],[18], Miranda[19]) and numerical investigations (Ekaterinas[20], Liu &Sankar[21]) has treated the effectiveness of active flow control as tool to delay boundary layer separation with particular regards to leading edge separation for the flap in multi component airfoil. Most of the time, principal goal applying this technique is the enhancement of take-off and landing aircraft performance. Our scope also is to verify numerically the effectiveness of such technique to increasing lift and delay or suppressing separation.

2. Case Setup

2.1. Geometry & Grid

The grid used for simulating the NACA0015 airfoil is generated by the GAMBIT program, and is shown in Figure 1. The grid extends from −10 chords upstream to 15 chords downstream. The airfoil geometry, slot positions, and dimensions are as follows. The chord length of the airfoil is 381mm, and a single jet with a width of 2.5% C is placed on the upper surface of airfoil and can be modeled as wall boundary condition (no control applied) or velocity inlet boundary condition (steady blowing) which simulating the blowing control under Re=455000 at the angles of attack 12º to 17º. The jet width is fixed at 2.5% chord length based on a study by Dannenberg and Weiberg[22]who showed that an increase of slot width beyond 2.5% C will not increase lift considerably. Three slot position is chosen, 10%C, 30%C & in 50% of chord length.

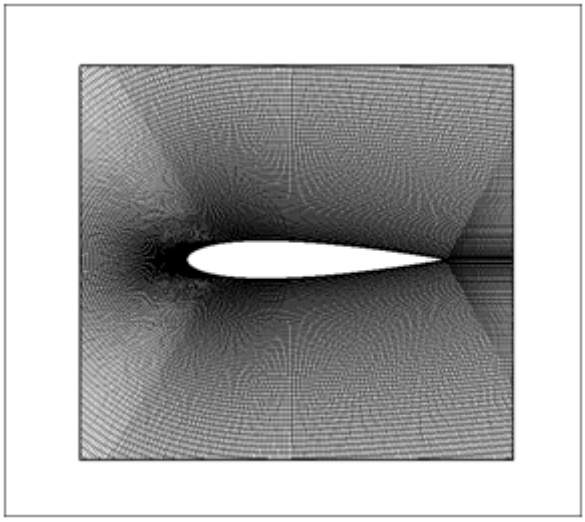

Figure 1. Structured "C" type grid used for NACA0015 CFD simulation

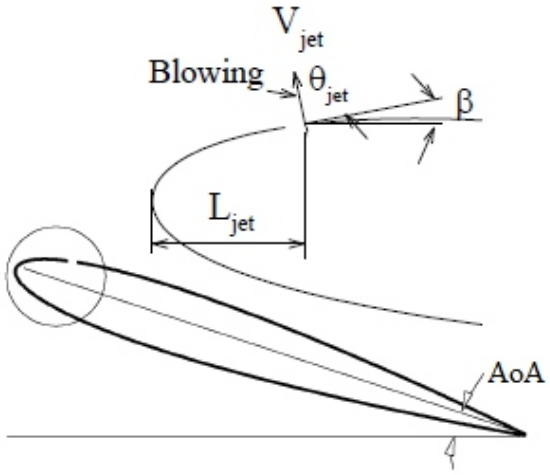

Figure 2. Blowing control mechanism

The grid shown is a "C" like structured grid. In order to resolve the boundary layer the mesh is refined on airfoil surface and over the blowing slots. The maximum aspect ratio of cells near the surface has been kept less than 50, and the first cell height has been fixed at 3*10-5 m (Y+≈1). Different size of grids are used to ensure grid independence of the calculated results until a stage is reached where the solution exhibits negligible change with further increase in the number of nodes. Consequently, the total number of cells is adopted as 180,000 cells.

2.2. Blowing Mechanism

As mentioned above blowing mechanism modeled as velocity inlet boundary condition and in this

study we want to investigate three different jet angles (0º, 30º, 45º) and three velocity ratios (1, 2, 6), to obtain this, jet velocity defined as

$$u = V * R * \cos(\theta_{iet} + \beta)$$
$$v = V * R * \sin(\theta_{jet} + \beta) \quad (2)$$

Where V is free stream velocity, R β is jet velocity ratio and is the angle between the free stream velocity direction and the local jet surface, θ_{jet} is the angle between the local jet surface and jet entrance velocity direction.

2.3. Governing Equations

In this review, because the Mach number is M ~ 0.05, the flow is incompressible. Also with regard to steady and two-dimensional condition governing equations will be as follows:

2.3.1. Continuity Equation

$$\frac{\partial u}{\partial x} + \frac{\partial v}{\partial y} = 0 \quad (3)$$

Where u and v are velocities in x and y directions respectively.

2.3.2. Momentum Equation

$$\rho u \frac{\partial u}{\partial x} + \rho v \frac{\partial u}{\partial y} = -\frac{\partial p}{\partial x} + \frac{\partial}{\partial y}\left[\mu\left(\frac{\partial v}{\partial x} + \frac{\partial u}{\partial y}\right)\right] \quad (4)$$

$$\rho u \frac{\partial v}{\partial x} + \rho v \frac{\partial v}{\partial y} = -\frac{\partial p}{\partial y} + \frac{\partial}{\partial x}\left[\mu\left(\frac{\partial v}{\partial x} + \frac{\partial u}{\partial y}\right)\right] \quad (5)$$

Where μ is dynamic viscosity, andis pressure.

2.3.3. Turbulence Model

The viscous model used for modeling the turbulence is Spalart-Allmaras. This model is a one equation model for the turbulent viscosity. It solves a transport equation for the kinematic eddy (turbulent) viscosity $\tilde{\upsilon}$. In its original form, the Spalart-Allmaras model is effectively a low-Reynolds number model and was designed specifically for aerospace applications involving wall-bounded flows and has been shown to give good results for boundary layers subjected to adverse pressure gradients.

The turbulent viscosity is computed from

$$\nu_T = \tilde{\nu} f_{v1},\ f_{v1} = \frac{\chi^3}{\chi^3 + c_{v1}^3},\ \chi = \frac{\tilde{\nu}}{\nu} \tag{6}$$

And the transport equation for $\tilde{\upsilon}$ is

$$\frac{\partial \tilde{\nu}}{\partial t} + u_j \frac{\partial \tilde{\nu}}{\partial x_j} = \frac{1}{\sigma} \frac{\partial}{\partial x_k} \left[\left(\nu + \tilde{\nu} \right) \frac{\partial \tilde{\nu}}{\partial x_k} \right] + c_{b1} \left(1 - f_{v2} \right) \tilde{S} \tilde{\nu} - c_{w1} f_w \left(\frac{\tilde{\nu}}{d} \right)^2 + \frac{c_{b2}}{\sigma} \frac{\partial \tilde{\nu}}{\partial x_k} \frac{\partial \tilde{\nu}}{\partial x_k} \tag{7}$$

More details about this equation can be found on reference[23].

2.4. Flow Solver

The freely-available prediction code, XFOIL and the commercial code, FLUENT were used detailed calculations. The Spalart-Allmaras fully turbulent model was used for modeling turbulence. The FLUENT code solves the Reynolds averaged Navier–Stokes equations using finite volume discretization. Second order upwind discretization in space is used, and the resulting system of equations is then solved using the SIMPLEC coupled solution procedure until convergence criteria of O (5) reduction in all dependent variable residuals is satisfied. Velocity inlet boundary conditions are used in the upstream and outer boundaries. Pressure outlet boundary condition is used in downstream and No-slip boundary conditions are used at solid surfaces. Low free stream turbulence levels are used to match the wind tunnel characteristics. A free stream turbulence level of $Tu = 0.1\%$ is used.

3. Validating Results

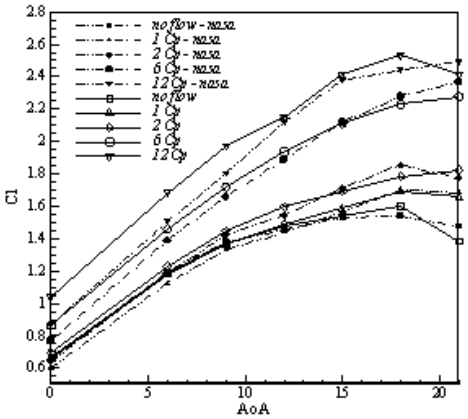

Figure 3. Comparison of the NASA experiment data and present work computational data for NACA84-M (L=32.5%C, W=0.333%C)

Mesh and the computational method described above were used to simulate NACA report no.385 first. Cause of using this report for validating the method is availability and comprehensiveness of its results. These results obtained over than 1200 different test condition which investigated the effect of parameters of the jet slot width, slot location, and air supply pressure inside the airfoil on aerodynamic properties of NACA84-Mairfoil, and has been published public. To ensure that we can simulate blowing effects correctly, the experiment was simulated in different conditions, and the result scan be seen in Figure 3.

Asseen in Figure 3, simulations show good agreement with experimental results and method is validated. Now we change the airfoil profile, and using the virtual wind tunnel created to investigate blowing effects on NACA0015airfoil.

4. Results & Discussion

The purpose of these simulations is to study the effects of jet location, jet angle and blowing ratio on NACA0015 airfoil aerodynamic coefficients and separation. To this end, more than 160 simulations were performed and the effect of these parameters was investigated.

Simulation results showed that with increasing angle of the jet relative to airfoil surface lift generated is also increasing. For example, when slot was in 10%C, blowing in angle 45º increasing the coefficient of lift to 3 times, but increasing the angle of jet significantly enhances the airfoil drag, sometimes up to 10 times of normal airfoil drag. Being able to simultaneously determine variations in lift and drag coefficients due to blowing the $\frac{L}{D}$ratio is used. The l/d Graph in Figure 4 is plotted for different angles of attack. As seen in the figure, the maximum amount of l/d ratios are for tangential states, so the best blowing angle is zero and next comparisons are done with the default tangential blowing.

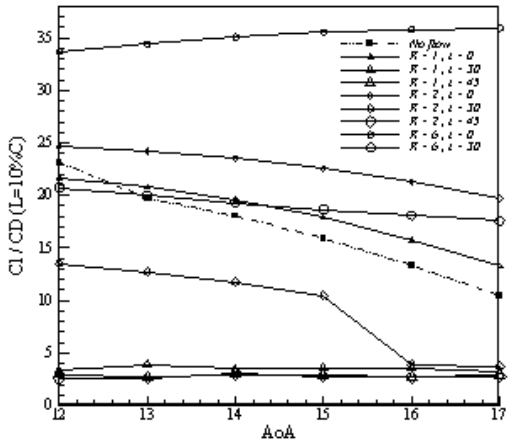

Figure 4. Comparison between L/D ratios of different blowing angles

Comparing simulation results to determine the most effective location for blowing was found that whatever the slot location became close to the trailing edge of the airfoil larger amount of lift is produced, this is because the starting vortex is produced, is more powerful. But this trend is reversed for the drag coefficient. Whatever Jet became much closer to the leading edge it became more effective and more reduction in drag can be seen. This is because the blowing has covered more surfaces and changing the velocity profiles in the boundary layer over more length of airfoil. Change of velocity profiles prevent of formation strong transverse velocity gradients in the boundary layer and according to the Newton's law of stress with a uniform velocity distribution shear forces are smaller and thus less friction drag is produced.

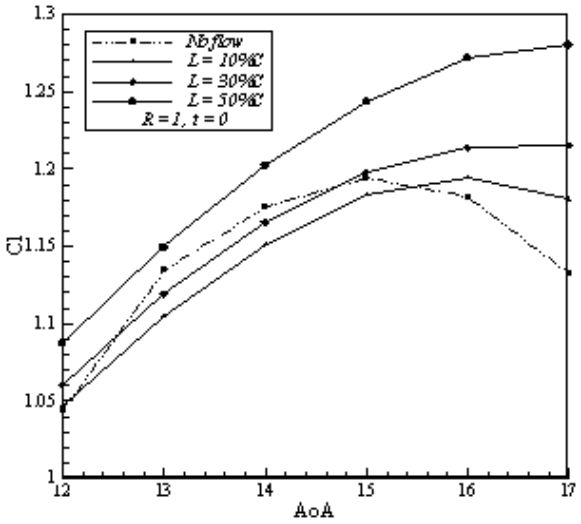

Figure 5. Effects of jet ratio and location on lift coefficient

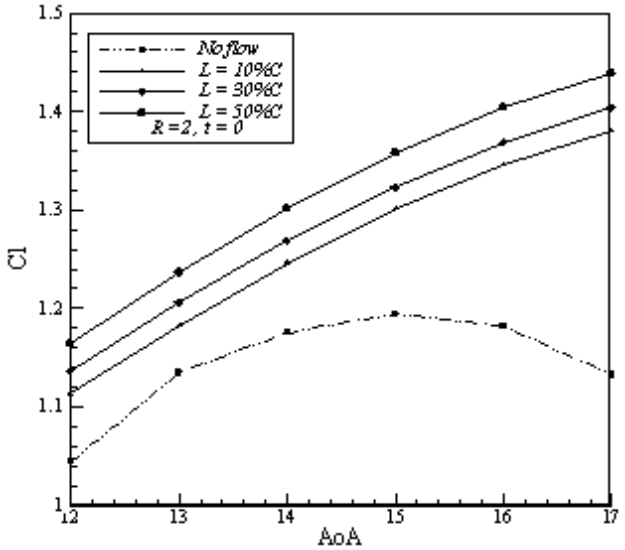

Figure 6. Effects of jet ratio and location on drag coefficient

Simulations shows that increasing the jet velocity has an amplifying effect on lift generation mechanism, but increasing jet velocity ratios does not have a uniform effect on drag coefficient and it seems there is a critical value that if jet velocity exceeds, higher ratios make more drag. In Figures 5 to 10 effects of jet location and blowing ratio is shown. The maximum change in lift is obtained by blowing at 50%C and the ratio of 6, which caused 80% increase in the coefficient of lift on the angle of attack 17º. The maximum reduction in the drag also obtained by blowing at 10%C and ratio of 6, which reduces drag coefficient about 45 percent in 17º.

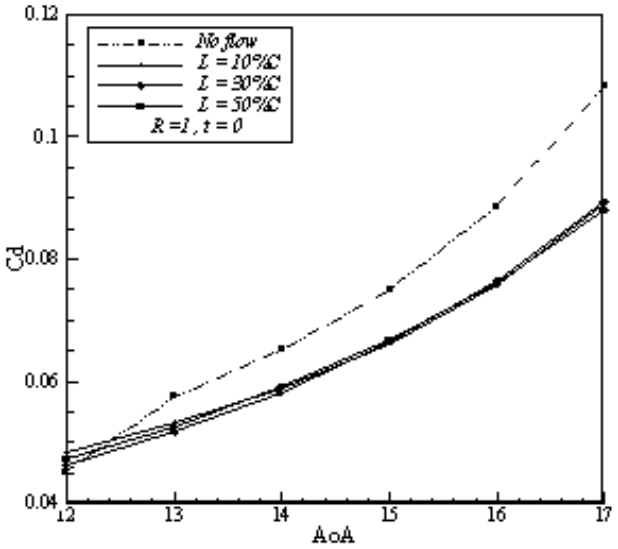

Figure 7. Effects of jet ratio and location on lift coefficient

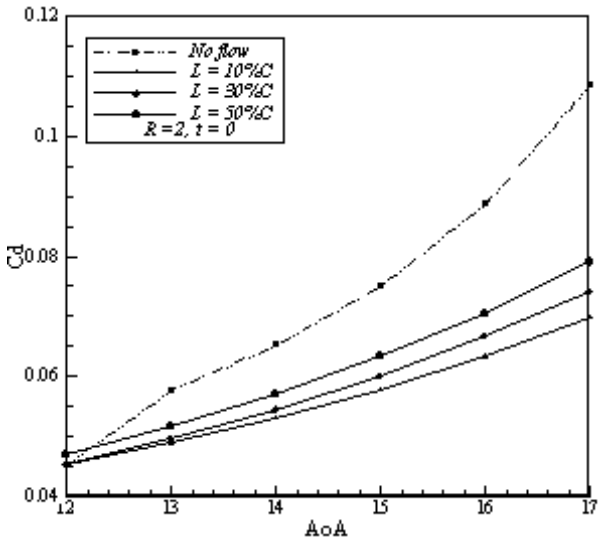

Figure 8. Effects of jet ratio and location on drag coefficient

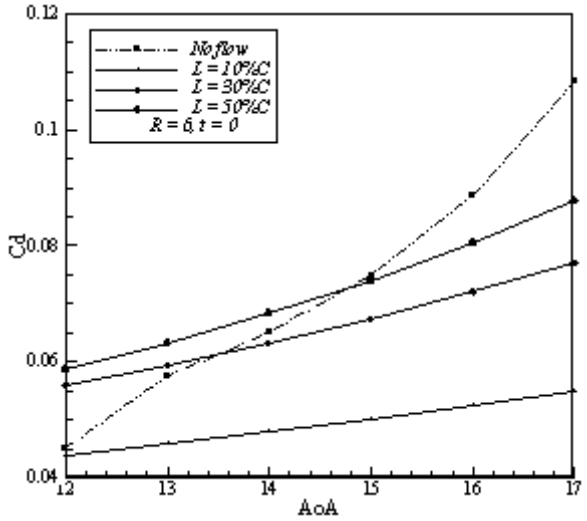

Figure 9. Effects of jet ratio and location on lift coefficient

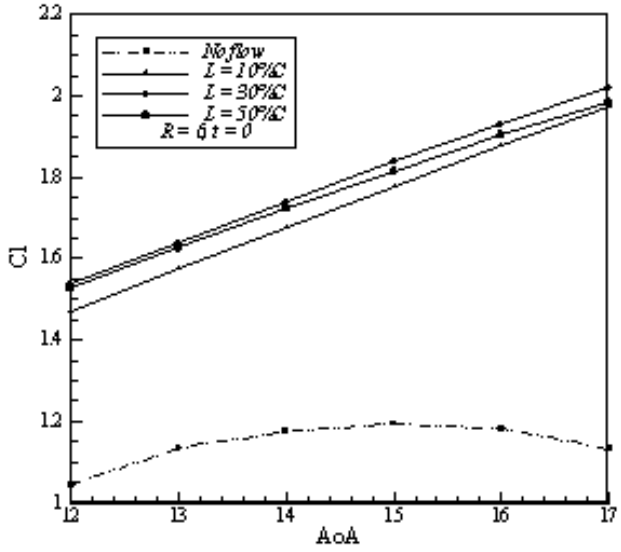

Figure 10. Effects of jet ratio and location on drag coefficient

Using blowing as a flow control method is an effective way to postponed separation over the upper side of airfoil. As the figures 5, 7 and 10 illustrate, applying blowing on the airfoil causes the stall angle to improve from 15º in the baseline case to higher angles of attack. Delaying separation upon the suction side of airfoil is an effective way to increase lift and decrease drag, because separation causes a significant loss of energy. Simulations show that by increasing the blowing ratio the separation point moves toward trailing edge. By increasing blowing ration higher amount of momentum injected to the retarded particles of boundary layerthat can't outcome any more against opposite pressure gradients.

Figures 11 to 14 shows streamline about NACA0015 airfoil in angle of attack 15º. In figure 11 separation of streamlines in rear side of airfoil can be seen but in figure 12 this area became smaller

(R=1) and in figures 13 and 14 we can see that separation area due to higher blowing ratios completely removed.

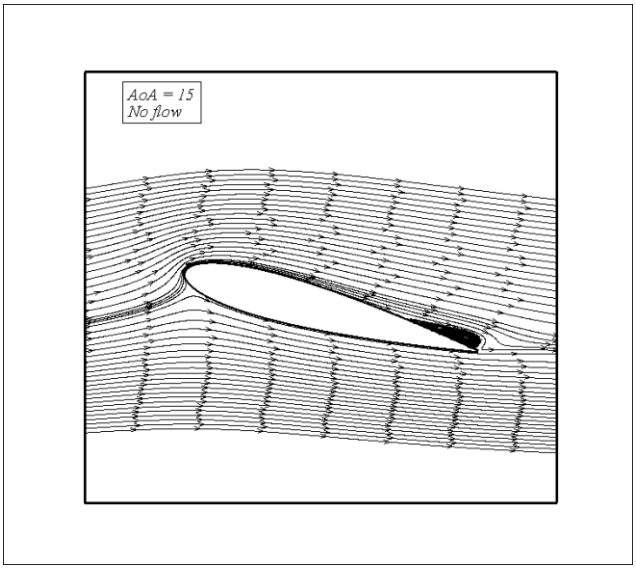

Figure 11. Streamlines for no blowing case at AoA 15º

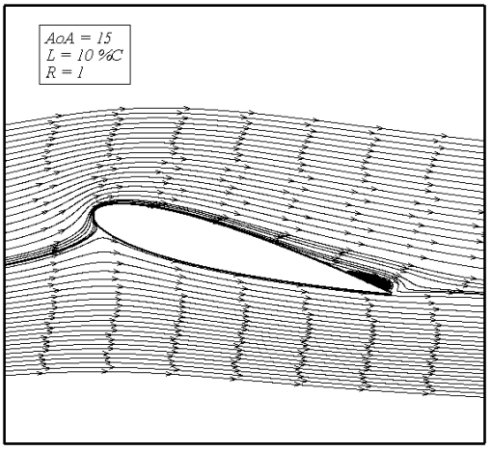

Figure 12. Streamline for blowing at L=10%C, R=1

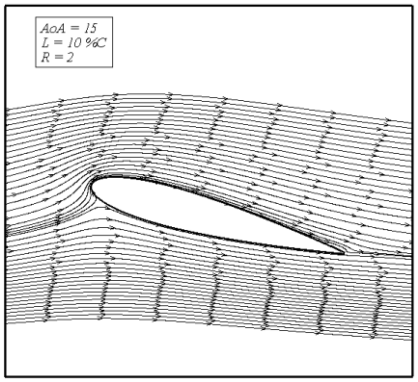

Figure 13. Streamline for blowing at L=10%C, R=2

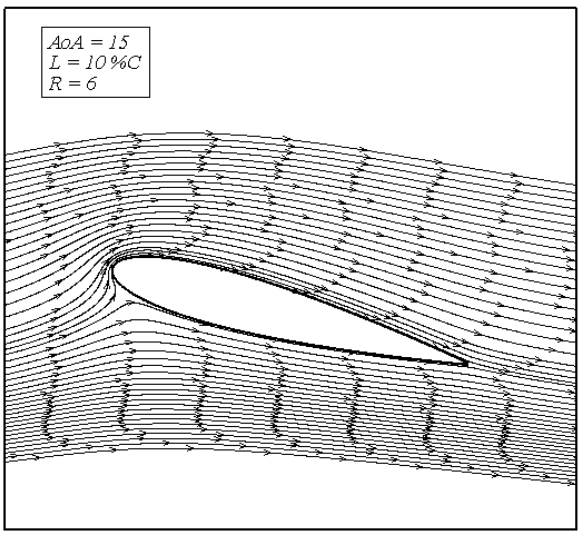

Figure 14. Streamline for blowing at L=10%C, R=6

5. Conclusions

In this study the effect of steady blowing on a NACA0015 airfoil at different ratios and jet locations at AoA of near stall has been investigated. Results of the simulations are in good agreement with experimental results. Through the investigation, the best jet angle is tangential because by increasing jet angle drag increases dramatically. Comparing different cases of applying blowing show that when the jet location is near the trailing edge, the lift coefficient increases more effectively. But this trend is reversed for the drag coefficient. Whatever Jet became much closer to the leading edge it became more effective and more reduction in drag occurs.

Simulations shows that increasing the jet velocity has an amplifying effect on lift generation mechanism, but increasing jet velocity ratios does not have a uniform effect on drag coefficient and it seems there is a critical value that if jet velocity exceeds, higher ratios make more drag. It was found that blowing has a significant effect on delaying separation on the upper side of the airfoil.

References

[1] Joslin, R.D. and D.N. Miller, Fundamentals and applications of modern flow control2009: American Institute of Aeronautics and Astronautics.

[2] Anders, S.G., W.L. Sellers, and A. Washburn, Active flow control activities at NASA Langley. AIAA paper, 2004. 2623(2).

[3] Miller, A.C., Flow control via synthetic jet actuation, 2004, Texas A&M University.

[4] Carnarius, A., et al. Numerical study of the optimization of separation control. 2007.

[5] Schetz, J.A., Foundations of Boundary layer theory for momentum, Heat, and Mass Transfer1984: Wiley Online Library.

[6] Bamber, M.J. and N.L.R. Center, Wind-tunnel Tests on Airfoil Boundary Layer Control Using a Backward-opening Slot1932: National Advisory Committee for Aeronautics.

[7] Poisson-Quinton, P.RecherchesTheoretiquesetExperimentalessur le Controle de la CoucheLimite. 1948.

[8] Lachmann, G.V., Boundary layer and flow control: its principles and application. Vol. 2. 1961: Pergamon.

[9] Gad-el-Hak, M., Flow control: passive, active, and reactive flow management2000: Cambridge Univ Pr.

[10] Katz, Y., B. Nishri, and I. Wygnanski, The delay of turbulent boundary layer separation by oscillatory active control, 1989, DTIC Document.

[11] Greenblatt, D. and I.J. Wygnanski, The control of flow separation by periodic excitation. Progress in Aerospace Sciences, 2000. 36(7): p. 487-545.

[12] Wong, C. and K. Kontis, Flow control by spanwise blowing on a NACA 0012. Journal of aircraft, 2007. 44(1): p. 337-340.

[13] Huang, L., et al., Numerical study of blowing and suction control mechanism on NACA0012 airfoil. Journal of aircraft, 2004. 41(5): p. 1005-1013.

[14] Schatz, M. and F. Thiele, Numerical study of high-lift flow with separation control by periodic excitation. AIAA paper, 2001. 296: p. 2001.

[15] Seifert, A., A. Darabi, and I.J. Wygnanski, Delay of airfoil stall by periodic excitation. Journal of aircraft, 1996. 33(4): p. 691-698.

[16] Tinapp, F. and W. Nitsche. On active control of high-lift flow. 1999.

[17] Wu, J., A. Vakili, and J. Wu, Review of the physics of enhancing vortex lift by unsteady excitation. Progress in Aerospace Sciences, 1991. 28(2): p. 73-131.

[18] Wu, J.Z., et al., Post-stall flow control on an airfoil by local unsteady forcing. Journal of Fluid Mechanics, 1998. 371(1): p. 21-58.

[19] Miranda, S., Active control of separated flow over a circular-arc airfoil, 2000, Citeseer.

[20] Ekaterinaris, J.A., Prediction of active flow control performance on airfoils and wings. Aerospace science and technology, 2004. 8(5): p. 401-410.

[21] Liu, Y., et al., Computational evaluation of the steady and pulsed jet effects on the performance of a circulation control wing section. AIAA paper, 2004. 56: p. 2004.

[22] Dannenberg, R.E. and J.A. Weiberg, Section Characteristics of a 10.5-Percent-Thick Airfoil with Area Suction as Affected by Chordwise Distribution of Permeability, 1952, DTIC Document.

[23] Spalart, P.R. and S.R. Allmaras, A one-equation turbulence model for aerodynamic flows. La rechercheaérospatiale, 1994. 1(1): p. 5-21.

Derivative Theorems of the Principle of Quasi Work

Ms. Shalini Negi

A B S T R A C T

Derivative theorems of Principle of Quasi Work, a powerful pseudo energy principle, are derived. These theorems, viz. Applied Load Theorem, Deflection Theorem and Unit Load Theorem are applicable to a pair of topologically similar structural systems. One more theorem referred to as Relative Deflection Theorem along with its two corollaries are also derived from this principle for facilitating truss analysis. Using these theorems, a new methodology for calculating nodal deflections of a truss from its internal member forces and vice versa is presented in this paper. This methodology is amazingly simple, easy, and fast. These theorems form the basis of present methodology. Thirteen nodal deflections of a four bay truss included in this paper were calculated by hand in less than fifteen minutes.

Keywords : Continuum Mechanics, Energy Methods, Structural Analysis, Truss Deflection, PQW, TSS, TST, TET

1. Introduction

All the presently available structural analysis procedures e.g. finite element methods ([1 - 4]) variational principles ([5, 6]) and energy methods([7, 8]), are meant for a single structure and do not provide any connection between two structural systems. The Principle of Quasi Work (PQW) derived by [6] establishes a connection between Topologically Similar Systems (TSS) in the realm of structural mechanics. PQW thus fills the existing void in the domain of structural mechanics. Theorems based on PQW which are useful for discrete structural modelshave been derived by [9, 10]. PQW was used advantageously by [9] and [11] for obtaining redundant reactions of beams. PQW has wide applicability as all the existing energy principles are derived as special cases of PQW by restricting TSS to Topologically Identical Systems (TIS), i.e. when two systems are identical with each other in every respect.

In this paper, four theorems and two corollaries are derived from PQW. Applied Load Theorem, Deflection Theorem and Unit Load Theorem are applicable to any two topologically similar structural systems. Applied Load Theorem is useful for obtaining loads acting on any given system by making use of the corresponding known deflections in its TSS. Similarly, Deflection Theorem and Unit Load Theorem are apt for calculating deflections of a given structural system by using the known solution of its TSS. A given system can be determinate or indeterminate whereas its TSS is invariably determinate

as its solution is used to solve the given problem. TSS of a given system can also be indeterminate as long as its solution is known. For a class of problem (e.g. beams, plates and shells) one TSS whose solution is known is sufficient to solve other problems in that class with much easecompared to solving it by classical methods.

The last derived theorem, Relative Displacement Theorem (RDT), and its corollaries considerably simplify the calculation of nodal deflections from internal member forces of determinate or indeterminate trusses. Internal member forces can also be calculated form nodal deflections by RTD in a simplified way. Some illustrations are also included. In the following section a brief introduction to PQW is given.

2. Principle of Quasi Work

The Principle of quasi work was first derived by [6] and subsequently stated by [7] and [8]. According to this principle quasi work (W_{mn}) done by a self equilibrating system of external forces, $\{P\}_m$, of a structural system (say 'm') while undergoing the corresponding compatible displacements, $\{d\}_n$, of the other topologically similar system (say 'n') is equal to the quasi strain energy(U_{mn}) due to internal forces, $\{F\}_m$, of the former system m while going through corre-sponding deformations, $\{\delta\}_n$, of the latter system n. In mathematical terms this can be stated as:

$$\{P\}_m^T \{d\}_n = \{F\}_m^T \{\delta\}_n \quad (1)$$

$$\text{OR} \qquad W_{mn} = U_{mn} \quad (2)$$

Where,

U_{mn} = Quasi strain energy= $\{F\}_m^T \{\delta\}_n$;

W_{mn} = Quasi work= $\{P\}_m^T \{d\}_n$;

$\{F\}_m$ = Internal member forces of the truss represented by TSS_m;

$\{P\}_m$ = External nodal loads on the truss represented by TSS_m;

$\{d\}_n$ = Displacement in TSS_n corresponding to $\{P\}_m$;

$\{\delta\}_n$ = Deformation of the member in TSS_n corresponding to $\{F\}_m$ in TSS_m;

$\{*\}^T$ = Transpose of $\{*\}$; m, n = Subscripts representing different TSS. (m, n = 1, 2…., $m \neq n$).

This principle establishes a link between two systems (m and n) which should satisfy the following three conditions:

1. Thesystems should be topologically similar. TSS, as explained by [9], have the same number nodes and similar nodal interconnectivity. It is self evident when discrete structural models or even trusses or

frames are involved, as in these cases nodes are well defined and hence the nodal interconnectivity is also obvious. In other cases of continuum structural elements it is not as obvious. All continuum structural elements can be considered as having infinite nodes (atoms or molecules) with well defined interconnectivity (forces between these). With this extension of definition of TSS, PQW can be applied to continuum elements like axial bars, torsion rods, beams, plates and other elements as well as to full fledged structures. Interestingly, what connects two nodes does not matter. In other words constitutive relations and material properties of the elements connecting different nodes have no place in the concept of TSS.

Detailed illustrations of TSS for discrete structural models, trusses and beams are given in [8 - 10].

2. Displacements and deformations of a TSS should be compatible within the system.

3. External forces acting on a TSS should be self equilibrating. Hence, all the reactions originating from the constraints form part of the external loads.

While applying this principle, attention has to be paid to the word 'corresponding' in the statement of PQW. For example take two axial bars (truss members) 'AB' and 'CD' of lengths 'L1' and 'L2'. As both the axial bars have infinite nodes, in these two axial bars end 'A' corresponds to end 'C' and end 'B' to end 'D'. In such cases, one has to resort to mapping in the two domains. For example, a point 0.64L1 from end 'A' in axial bar 'AB' will have its corresponding point at 0.64L2 from end 'C' in axial bar 'CD'.

3. Derivative Theorems of PQW

From PQW, theorems which are useful for calculating loads and deflections in topologically similar structural systems are derived hereunder. In PQW, the problem at hand represents one of the systems and its topologically similar system is exclusively the choice of the analyst. In these theorems, loads include moments and deflections include rotations; i.e., the terms 'loads' and 'deflections' are used in a generalized sense.

3.1. Load Theorem for Topologically Similar Structures

This theorem relates two TSS and can be used to find the load acting at a point in a system with the help of deflection at its corresponding point in another TSS.

STATEMENT: *"In a pair of Topologically Similar Systems (m and n); gradient of Quasi Strain Energy / Quasi Work with respect to deflection at any point in one of the systems (say n) is equal to load acting*

at the corresponding point in the other system (m)and is in the direction of the displacement."

In mathematical form, this is stated as:

$$\frac{\partial U_{mn}}{\partial d_{jn}} = \frac{\partial W_{mn}}{\partial d_{jn}} = P_{jm} \qquad j = 1, 2, ..., N \tag{3}$$

PROOF: From the definition of PQW we have:

$$U_{mn} = W_{mn} = \{P\}_m^T \{d\}_n \tag{4}$$

The gradient of U_{mn} (Eqn.4) with respect to displacement d_{jn} yields Eqn.(3).

3.2. Deflection Theorem for Topologically Similar Structures

This theorem relates two TSS and is used to determine deflection at any desired point in one system with the help of load acting at the corresponding point in second system.

STATEMENT: *"In a pair of Topologically similar systems (m and n); gradient of Quasi Strain Energy / Quasi Work with respect to a point load acting in one of the systems (say m) is equal to the deflection in the direction of the point load at the corresponding point in the other system (n)."*

$$\frac{\partial U_{mn}}{\partial P_{jm}} = \frac{\partial W_{mn}}{\partial P_{jm}} = d_{jn} \qquad j = 1, 2, ..., N \tag{5}$$

PROOF: The gradient of U_{mn} (Eqn.4) with respect to force P_{jm} yields Eqn. (5).

Eqns. (3 and 5) have forms similar to the familiar Castigliano's theorems except that these govern a pair of two topologically similar systems and the concept of complimentary energy does not exist in PQW. It shall be realized that when the pair of systems are restricted to be TIS (i.e., these are clones of each other), these equations produce the same results as those due to Castigliano's theorems; thereby, establishing the fact that the present theorems are more general forms of the statement of these classical theorems.

When in any two TSS structural stiffness (e.g., AE/ GJ/ EI) is the samethen these systems are designated by Topologically Equivalent Systems, (TES), and for these systems, Eqn.(5) becomes:

$$\frac{\partial W_{mn}}{\partial P_{jm}} = \frac{\partial U_{mn}}{\partial P_{jm}} = \frac{\partial U_{nm}}{\partial P_{jm}} = \frac{\partial W_{nm}}{\partial P_{jm}} = d_{jn} \qquad j = 1, ..., N \tag{6}$$

3.3. Unit Load Theorem for TSS

Unit load theorem is used to obtain deflections in one system by applying a unit load in the other TSS.

STATEMENT: *"In a pair of Topologically similar sys-tems (m and n); Quasi Strain Energy / Quasi Work with respect to a unit load in one of the systems (say m) is equal to the deflection in the direction of the unit load at the cor-responding point in the other system (n)."*

In mathematical form, it is stated as:

$$\bar{U}_{mn} = \bar{W}_{mn} = d_{jn} \tag{7}$$

Where, are $\bar{U}_{mn}$ and $\bar{W}_{mn}$ U_{mn} and W_{mn} for a unit load applied in TSS_m.

PROOF: If in TSS_m only one load acts at the location '*j*' and if this load is equal to unity then $\{P\}_m^T = P_{jm}$ (= 1). In such a case, PQW takes the following form

$$\bar{U}_{mn} = \bar{W}_{mn} = \{P\}_m^T \{d\}_n = P_{jm} d_{jn} = d_{jn} \tag{8}$$

This completes the proof. For TES, Eqn.(7) takes the form

$$\bar{W}_{mn} = \bar{U}_{mn} = \bar{U}_{nm} = \bar{W}_{nm} = d_{jn} \tag{9}$$

4. Relative Deflection Theorem for Trusses

A theorem for calculating relative deflection of two nodes with respect to each other connected by a truss member is stated and proved. This theorem significantly simplifies the calculations needed for obtaining nodal deflections and member forces of any determinate or indeterminate truss.

STATEMENT: "In a given truss the relative displacement '$d_{i/j}$' of any two nodes 'i' and 'j' is equal to the deformation 'δ_k' of the truss member 'k' connecting these two nodes and is along the axis of the truss member."

In mathematical form it can be written as:

$$d_{i/j} = d_i - d_j = \delta_k \ (= F_k L_k / A_k E_k) \tag{10}$$

PROOF: Take a truss having 'N' nodes with 'M' axial members. For any given self equilibrating loading, let F_n be the internal force in these truss members. This given truss is denoted by TST_1. A topologically similar truss, TST_2, is derived from the given truss by assigning zero stiffness to all truss members except one member 'k' which connects nodes '*i*' and '*j*'. Let this member carry a self equilibrating tensile load 'P_2'. Load acting at node '*i*' will be taken as positive and hence load at node '*j*' will be negative. The force $\{F_k\}_2$ in this member is equal to P_2.

Quasi work $W_{21} = \{P_2\}_2 \{d_i\}_1 - \{P_2\}_2 \{d_j\}_1$
$= \{P_2\}_2 (\{d_i\}_1 - \{d_j\}_1)$ (11)

Quasi strain energy $U_{12} = \{P_2\}_2 \{\delta_k\}_1$ (12)

PQW ($W_{21} = U_{21}$) yields Eqn.(10) after dropping curly brackets along with suffix '1'.

4.1. Corollary - 1:

"The relative displacement of the last node with respect to the first node in collinearly connected 'n' truss members in series is equal to the sum of the individual deformation of these 'n' truss members and is along their axes."
In mathematical form it can be stated as:

$$d_{(n+1)/1} = d_{(n+1)} - d_1 = \sum_{j=1}^{n} \delta_j = \sum_{j=1}^{n} \frac{F_j L_j}{A_j E_j} \quad (13)$$

PROOF: Relative displacement between nodes of different elements is given by:

$$d_{(n+1)/n} = d_{n+1} - d_n = \delta_n = F_n L_n / A_n E_n \quad (14)$$

$$d_{n/(n-1)} = d_n - d_{n-1} = \delta_{n-1} = F_{n-1} L_{n-1} / A_{n-1} E_{n-1} \quad (15)$$

$$d_{3/2} = d_3 - d_2 = \delta_2 = F_2 L_2 / A_2 E_2 \quad (16)$$

$$d_{2/1} = d_2 - d_1 = \delta_1 = F_1 L_1 / A_1 E_1 \quad (17)$$

As these are connected in series with their axes collinear, the sum of all these equation yields Eqn.(13).

4.2. Corollary - 2:

"In collinearly connected 'n' truss members of a truss whose first and last nodes are constrained, the deformation (and thus internal force) of at least one truss member is opposite in nature to the deformation of other 'n-1' members."

PROOF: From corollary - 1, displacement of the last node with respect to the first node is zero as both these nodes are constrained. Hence,

$$d_{(n+1)/1} = d_{(n+1)} - d_1 = 0 = \sum_{j=1}^{n} \delta_j = \sum_{j=1}^{n} \frac{F_j L_j}{A_j E_j} \qquad (18)$$

The last two sums in Eqn.(18) can not be zero unless at least one member deformation in the first sum and at least one member force in the second sum is of opposite sign.

Relative displacement theorem and its corollaries simplify the procedure for calculating nodal deflections and member forces in any given truss. To illustrate the use of the given theorem and its corollary three illustrations shown in Figs. 1-3 follow.

5. Nodal Deflections of Trusses

In this section, three examples are chosen to illustrate the procedure of obtaining nodal deflections of trusses. These illustrations are depicted in Fig.1 to Fig.3. Fig.1 shows a three bay truss with one internal and one external indeterminacy. Fig.2 depicts a four bay truss with two degree internal indeterminacy and one-degree of external indeterminacy. Fig.3 shows a two storey truss with two-degree internal indeterminacy. In what follows, nodal deflections (u and v) of the given truss (TSS1) are represented by dropping suffix '1'.

Fig. 1. Three bay truss

Fig.1a depicts a three bay truss A_1 B_1...F_1 having one internal and one external degree of indeterminacy is solved for nodal deflections. Young's modulus of elasticity,'E', for all members is 205 kN/mm2. This given truss isdesignated by TST1. Member forces are obtained by any convenient conventional method after which nodal deflections are obtained by using RDT and its corollaries in the following manner. Let

u_* = Horizontal deflection of truss joint '*' (* represents: A, B, C, ...).

v_* = Vertical deflection of truss joint '*' (* represents: A, B, C, ...).

From the given support conditions $u_a = v_a = v_c = v_d = 0$. Now utilizing RTD and its corollaries, horizontal deflection of nodes 'B1', 'C1', 'D1' and vertical deflection of node 'F1' are calculated as follows:

$u_b - u_a = \delta_{ab} = 0.2179$ mm (from Table1, Column 6) which yields $u_b = 0.2179$ mm. Similarly, $u_c = \delta_{ab} + \delta_{bc} = 0.3912$ mm, $u_d = u_c + \delta_{cd} = 0.4757$mm and $v_f = \delta_{cf} = -0.2335$ mm.

In order to calculate other nodal deflections (i.e.,v_b, u_e, v_e, and u_f) by utilizing RDT, vertical deflection of node 'E' or 'B'and horizontal deflection of node 'E' or 'F' should be known. Here let us choose to calculate deflections (u, v) of node 'E' by using deflection theorem for which TST_2 has to be defined.

Fig.1b shows TST_2which is derived from the given truss by assigning zero stiffness (AE = 0) to all truss members connected to nodes D_1 and F_1. Thus TST_2 is a determinate truss $A_2B_2C_2E_2$ having only five members. Loads on TST_2 are applied at those nodes whose deflection is to be calculated. Hence, at node 'E_2' a horizontal load P1kN and avertical load P_2kN are applied as the deflection in these direction is to be calculated. Internal forces in truss members of TST_2 are given in column 7 of Table 1. Column 8 of the table gives contribution of truss members to U_{21} and the sum of this column given in the last row is equal to U_{21}. By using the deflection theorem the deflections of node 'E_1' are $u_e = \partial U_{21} / \partial P_1 = 0.3349$ mm and $v_e = \partial U_{21} / \partial P_2 = -0.2474$ mm.

Other two nodal deflections (v_b and u_f) are once again obtained by relative deflection theorem. $v_e - v_b = \delta_{eb} = -0.0661$ which yields $v_b = -0.1813$ mm. Similarly, $u_f = 0.4252$ mm. All these nodal deflections (in mm) are summarized below:

$u_a = 0$, $v_a = 0$; $u_b = 0.218$, $v_b = -0.181$; $u_c = 0.391$, $v_c = 0$;$u_d = 0.476$, $v_d = 0$; $u_e = 0.335$, $v_e = -0.247$ and $u_f = 0.425$, $v_f = -0.234$. These values are the same as obtained by conventional methods.

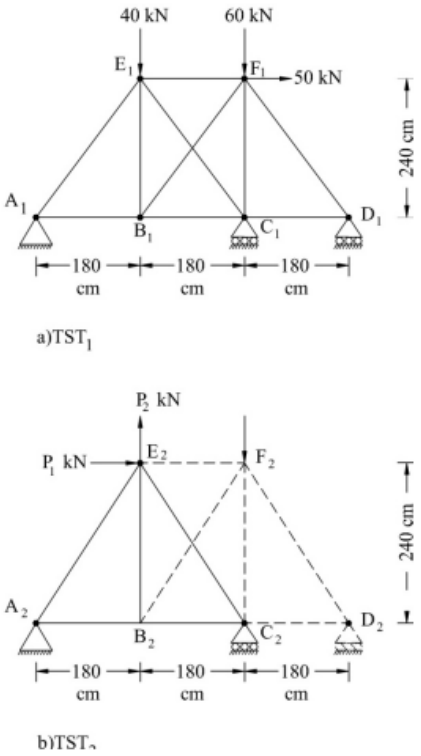

Figure 1. Three bay Truss

Thus, once member forces of a truss are known, the present method makes it possible to calculate all the nodal deflections easily and quickly without any need of a computer. In fact, all the above nodal deflections were obtained in about ten minutes by hand calculation with the help of a business pocket calculator.

Table 1. Calculations for the Three Bay Truss Shown in Fig.1a

Given Truss (Fig. 1a):: TST_1						Chosen Truss : (Fig.1b) :: TST_2	
MEMBER No.'j'	Nodes	A_j cm^2	L_j cm	Internal Force $\{F_j\}_1$:: kN	Deformation $\{\delta_j\}_1=\{F_jL_j/A_jE\}_1$	Internal Force: $\{F_j\}_2$kN	Individual contribution to U_{21} :: $\alpha_j = \{\delta_j\}_1 \{F_j\}_2$
1	A_nB_n	20	180	49.6299	0.2179	$0.5\ P_1 - 0.375\ P_2$	$0.1089P_1 - 0.0817P_2$
2	B_nC_n	20	180	39.4628	0.1733	$0.5\ P_1 - 0.375\ P_2$	$0.0866P_1 - 0.0650\ P_2$
6	C_nD_n	20	180	19.2598	0.0845	0	0
3	E_nF_n	20	180	20.5731	0.0903	0	0
4	B_nE_n	24	240	-13.5561	-0.0661	0	0
5	C_nF_n	24	240	-47.8764	-0.2335	0	0
7	A_nE_n	30	300	61.6855	0.0030	$5P_1/6 + 0.625\ P_2$	$0.0025\ P1 + 0.0019\ P_2$
8	B_nF_n	30	300	19.9451	0.0827	0	0
9	D_nF_n	30	300	-32.0996	-0.1566	0	0
10	C_nE_n	30	300	-33.6717	-0.1643	$-5P_1/6+0.625P_2$	$0.1369P_1 - 0.1026\ P_2$
					U_{21} = SUM of α_j (for j = 1...10) =		$0.3349P_1 - 0\ .2474P_2$

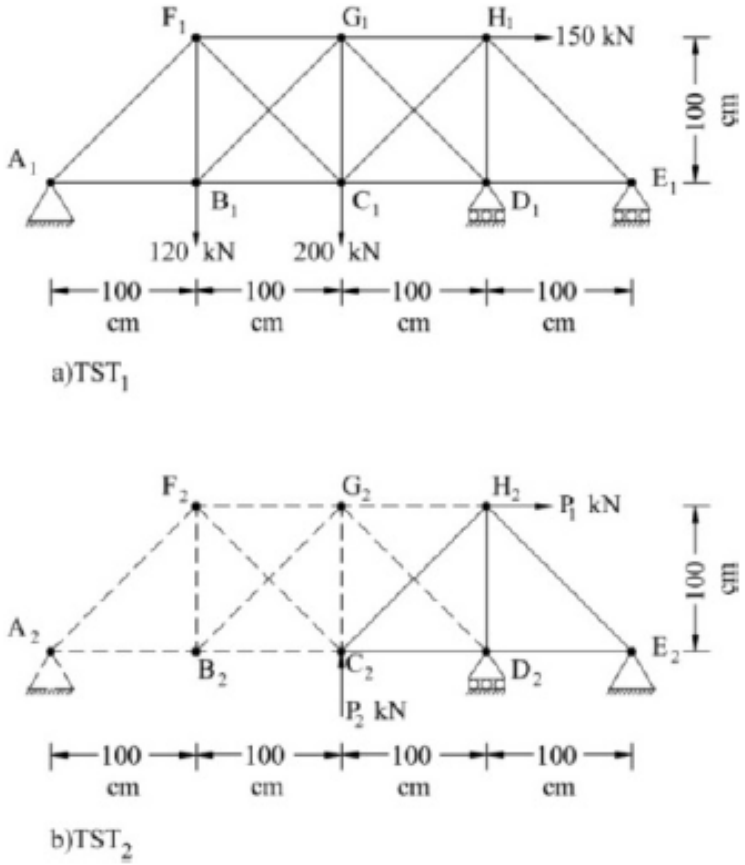

Fig. 2. Four bay truss

Fig.2a depicts a four bay truss '$A_1B_1...H_1$' with two- degree internal and one- degree external indeterminacy is taken for illustrating the use of PQW and relative deflection theorem. E for all members is E = 205kN/mm^2.From the given support conditions $u_a = v_a = v_d = v_e = 0$. Horizontal deflection of nodes 'B_1', 'C_1', 'D_1', 'E_1' and vertical deflection of node 'H_1' are obtained as follows. From relative deflection theo- rem, $u_b - ua = \delta_{ab} = 0.2344$ (column 6 of Table 2) which yields $u_b = 0.2344$ mm. Utilizing corollary of relative de- flection theorem, $u_c - u_a = \delta_{ab} + \delta_{bc} = 0.4193$ mm, which gives $u_c = 0.4193$ mm. Similarly, $u_d = 0.5046$ mm, $u_e = 0.4859$ mm and $v_h = -0.1388$ mm. For calculating other deflections in the above manner, horizontal deflection of any- one among 'F_1','G_1' and 'H_1' nodes and vertical deflection of one among 'B_1','C_1','F_1', and 'G_1' must be known. Let us choose to calculate u_h and v_c. These will be obtained by using PQW for which TST_2 along with loading and supports are chosen as shown in Fig. 2.

All members connected to nodes A_2, B_2 and G_2 are as- signed zero stiffness and the roller support at E_1 in TST_1 is replaced by a pinned support. Internal member forces in TST_2 are given in column7 of Table 2. Last column ofTable2 gives contribution of truss members to U_{21} and the sum of this column (in the last row) gives U_{21}.

By using deflection theorem $v_c = \partial U_{21}/ \partial P_2 = - 0.6038$ mm. Node 'E' has a horizontal reaction equal to $-P_1$, hence$\partial U_{21}/ \partial P_1 = u_h - u_e = -0.1917$ mm which yields $u_h = 0.2942$ mm. Now relative displacement theorem yields $u_g = 0.2493$, $u_f = 0.3579$ mm and $v_g = -0.5494$ mm.

Table 2. Nodal Deflection Calculations for the Four Bay Truss Shown in Fig.2a

Given Truss (Fig. 2a):: TST1						Chosen Truss :: (Fig.2b) :: TST2	
MEMBER		Aj cm^2	Lj cm	Internal Force {Fj}1: kN	Deformation	Internal Force:	Individual contribution to U21 :: áj = {äj}1 {Fj}2
No.'j'	Nodes				{äj}1 = {FjLj / AjE}1	{Fj}2kN	
1	AnBn	50	100	240.2813	0.2344	0	0
2	BnCn	50	100	199.5042	0.1849	0	0
3	CnDn	50	100	87.4107	0.0853	P2	0.0853 P2
4	Dn En	50	100	-19.158	-0.0189	P2	-0.0187 P2
5	FnGn	50	100	-111.3385	-0.1086	0	0
6	GnHn	50	100	46.0073	0.0449	0	0
7	BnFn	50	100	69.2229	0.0675	0	0
8	CnGn	50	100	55.7916	0.0544	0	0
9	DnHn	50	100	-142.3093	-0.1388	P1+ 2 P2	-0.1388P1 - 0.2777 P2
10	AnFn	50	141.42	-127.6762	-0.1762	0	0
11	En Hn	50	141.42	27.0934	0.0374	-1.4142 (P1+P2)	- 0.0529P1 - 0.0529P2
12	BnGn	50	141.42	71.8097	0.0991	0	0
13	DnGn	50	141.42	-150.7109	-0.2079	0	0
14	CnFn	50	141.42	-29.7802	-0.0411	0	0
15	CnHn	50	141.42	174.1621	0.2403	-1.4142 P2	-0.3398P1
			U21 = SUM of áj (for j = 1...10) =				- 0.1917P1- 0.6038P2

The last two unknown deflections, v_f and v_b, are calculated either using PQW (for which another TSS which includes node 'F' or 'B' is to be chosen) or by observing that u_f and the displacement of node 'F' along AF (δ_{af}) are already known. From these data one can obtain v_f as follows. Let u_{1f} and v_{1f} be the displacements of node 'F' along and perp endicular to the axis of member 'AF'.In that case, $u_f = u_{1f}$ Cos 45^0 - v_{1f} Sin 45^0 and $v_f = u_{1f}$ Sin 45^0 + v_{1f} Cos 45^0. These two equations with $u_{1f} = \delta_{af}$=-0.1762 and u_f = 0.3579 yield v_f=-0.6071 mm and v_{1f} = -0.6823. Again, using the relative dis- placement theorem, $v_f - v_b = \delta_{bf}$ which gives v_b = -0.6746 mm. All these nodal deflections (in mm) are summarized below:

$u_a = 0$, $v_a = 0$; $u_b = 0.234$, $v_b = -0.675$; $u_c = 0.419$, $v_c = -0.604$; $u_d = 0.505$, $v_d = 0$; $u_e = 0.486$, $v_e = 0$; u_f = 0.358, v_f = -0.607; u_g = 0.249, v_g = -0.549 and u_h = 0.294, v_h = -0.139.

These values are the same as obtained by conventional methods.

Fig.3: Two storey truss

In this illustration, Fig. 3a, a two storey truss '$A_1B_1...F_1$'

having two degree internal indeterminacy is solved for nodal deflections. It is pinned at joint 'A_1' and has a roller support at joint 'B_1'.

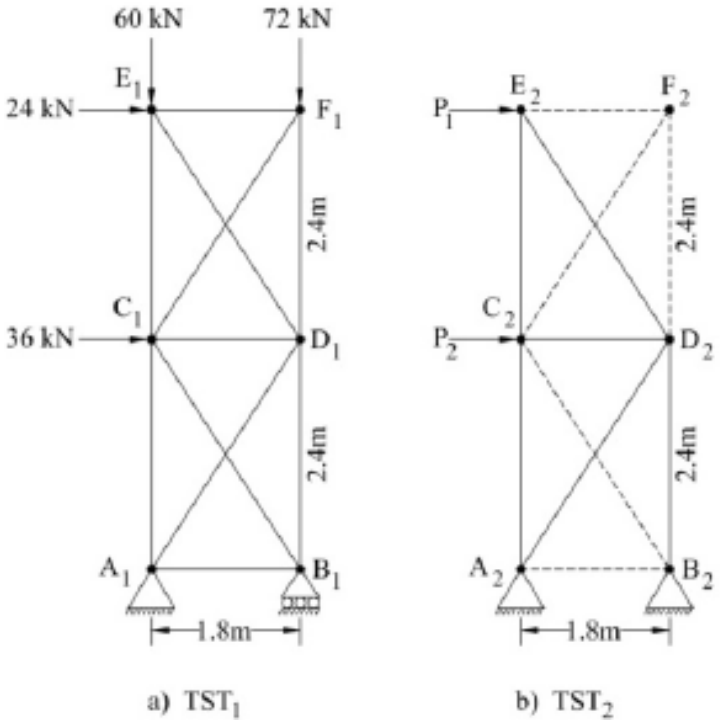

Figure 3. Two Storey Truss

Table 3. Nodal Deflection Calculations for theTwo Storey Truss Shown in Fig.3a

Given Truss (Fig. 3a):: TST1						Chosen Truss :: (Fig.3b) :: TST2	
MEMBER		Aj cm^2	Lj cm	Internal Force	Deformation	Internal Force:	Individual contribution to U21 : áj = {äj}1 {Fj}2
No.'j'	Nodes			{Fj}1::kN	{äj}1 = {FjLj / AjE}1	{Fj}2kN	
1	AnBn	10	180	41.686	0.3752	0	0
2	CnDn	10	180	11.877	0.107	0	-0.10689 P2
6	En Fn	10	180	6.1911	0.0557	0	0
3	An Cn	20	240	27.582	0.1655	1.3333 P1	0.22066P1
4	CnEn	20	240	-19.745	-0.1185	1.3333 P1	-0.158P1
5	BnDn	20	240	-128.42	-0.7705	-2.667 P1 -1.333 P2	2.05472P1+1.02736P2
7	DnFn	20	240	-63.745	-0.3825	0	0
8	AnDn	30	300	30.523	0.1526	1.667P1 + 1.667P2	0.25436P1+0.254358P2
9	DnEn	30	300	-50.318	-0.2516	-1.667 P1	0.41932P1
10	BnCn	30	300	-69.477	-0.3474	0	0
11	CnFn	30	300	-10.319	-0.0516	0	0
					U21 = SUM of áj (for j = 1...10) =		2.79109P1 + 1.174825P2

Table 4. Member Force calculations for truss shown in Fig.3a

Deflection of the Nodes of the given Truss							
Nodes		A1	B1	C1	D1	E1	F1
Hor. Def. ui		0	0.37517	1.1748	1.2817	2.7911	2.8468
Vert. Def. vi		0	0	0.16549	-0.77052	0.04702	-1.153
Member Data and Internal Force Calculations for Truss Members							
No. 'j'	Nodes	Length (Lj) mm	Area (Aj) mm^2	Deformation		Fj = A E äj / L(kN)	
				By Deflection Theorem	äj (mm)		
1	A1 B1	1800	1000	ub - ua	0.3752	4	1.686
2	C1 D1	1800	1000	ud - uc	0.1067	1	1.877
3	E1 F1	1800	1000	uf - ue	0.0557	6	0.1911
4	A1 C1	2400	2000	vc - va	0.1655	2	7.582
5	C1 E1	2400	2000	ve - vc	-0.1185	-19.745	
6	B1 D1	2400	2000	vd - vb	-0.7705	-128.42	
7	D1 F1	2400	2000	vf- vd	-0.3825	-63.745	
8	A1 D1	3000	3000	3/5 ud + 4/5 vd	0.1526	3	0.523
9	D1 E1	3000	3000	(-3(ue - ud) + 4*(ve -vd)) / 5	-0.2516	-50.318	
10	B1 C1	3000	3000	(-3(uc- ub) + 4*(vc - vb)) / 5	-0.3474	-69.477	
11	C1 F1	3000	3000	(3(uf - uc) + 4*(vf - vc)) / 5	-0.0516	-10.319	

E for all members is E = 200kN/mm^2. From support conditions $u_a = v_a = v_b = 0$. By using relative displacement theorem and its corollary we have:

$v_c = \delta_{ac}$ =0.165492 mm; $v_e = \delta_{ac} + \delta_{ce}$ = 0.047022 mm; $v_d = \delta_{bd}$ = -0.77052 mm; $v_f = v_d + \delta_{df}$ = -1.15299 mm and u_b = 0.375174 mm.

In order to calculate horizontal deflection of nodes 'C_1', 'D_1', 'E_1' and 'F_1' by using relative displacement theorem, we need to know the horizontal displacements of one node each from the pair 'C', 'D' and 'E', 'F'. Let us chose to calculate the deflection of nodes 'C' and 'E'. This can be easily calculated by resorting to PQW for which TST_2 is to be chosen which should include the nodes 'C' and 'E' and is a stable truss under the chosen loading conditions. Fig. 3b shows one such TST_2.

Loads 'P_1' and 'P_2' are applied at the nodes and in the direction in which the deflection is to be calculated. Member forces in TST_2 are given in column 7 of Table 3. In column 8 are tabulated the contribution from individual members to U_{21} in terms of P_1 and P_2. The last row gives the value of U_{21}, which is the sum of all these individual contributions. The partial derivative of U_{21} with respect to P_1 and P_2 yields the values of u_e = 2.79109 mm and u_c = 1.174825 mm, respectively. Now by using RDT one can easily calculate u_d = 1.281718 mm and u_f = 2.8468099 mm. Deflection of different nodes in mm is summarized in second and third row of Table 4 and these values are same as obtained by conventional methods.

Thus one can observe that obtaining displacement of joints once the member forces are known is very easy compared to any conventional method.

6. Member Forces of Trusses

In this section member forces will be calculated from the given nodal deflections. The procedure adopted is simple and fast. All the calculations can easily be carried out using a pocket calculator. All this is possible because of the rela- tive deflection theorem.

For illustrating the procedure the example in Fig.3 is again used. Here, starting point is the nodal displacements given in 2nd and 3rd row of Table 4. From these deflections internal forces in the members are calculated. In column 5 of Table 4 are given relations for member deformations got from RTD and column 6 gives their numerical values. In the last column member forces are tabulated, which are the same as given in Table 3 column 5.

7. Conclusions

1. PQW is successfully applied to a set of any two axial bars (Truss members).
2. Three theorems are derived from PQW. Deflection theorem and unit load theorem are useful for obtaining deflection in topologically similar structures. Their use has been illustrated for trusses.
3. Relative deflection theorem and its corollaries are de- rived from PQW for obtaining nodal deflections of trusses. These theorems greatly simplify the procedure for obtaining nodal deflection from given member forces.
4. In case of trusses, topologically similar trusses for a given problem can be chosen in such a way so as to minimise effort needed to solve the given problem. The chosen truss is derived from the given truss by assigned zero stiffness (AE) to some of the truss members in such a way so that the derived truss is determinate and remains stable under the chosen loading.
5. The concepts of virtual force and complementary energy do not exist in PQW as both the systems are real. Hence, no additional effort is needed for learning this method.

References

[1] Akin, J.E., Finite Elements for Analysis and Design, Aca- demic Press, London, 1994.

[2] Zienkiewicz, O. C. and Taylor, R. L., The Finite Elements Method, McGraw Hill, 1989.

[3] Rao, S. S., The Finite Element Method in Engineering, Pergamon Press, 1989.

[4] *Cook, R.D., Malkus, D.J. and Plesha, M.E. Concepts and Applications of Finite Element Analysis, John Wiley & sons, New York, 1989.*

[5] *Reissner, E., "Formulations of variational theorems in geometrically non-linear elasticity." Journal of Engineering Mechanics, vol. 110(9), pp. 1377 – 1390, 1984.*

[6] *Reissner, E., "On mixed variational formulations in finite elasticity." Acta Mech., vol. 56(3-4), pp. 117-125, 1985.*

[7] *Argyris, J. H. and Kelsey, S., Energy Theorems and Structural Analysis, Butterworth & Co. Ltd., 1960.*

[8] *Shames, I. A. and Dym, C. L., Energy and Finite Element methods in Structural Mechanics, McGraw – Hill Book Co., 1985.*

[9] *Panditta, I.K., Some Studies on Computer Aided Model Based Design, Ph. D. Thesis, Department of Aerospace Engineering, Indian Institute of Technology Bombay, India, 1996.*

[10] *Panditta, I.K., Shimpi, R.P. and Prasad, K.S.R.K. (1999), "On the theory of discrete model analyses and design." Interna- tional Journal of Solids and Structures, vol. 36, pp. 2443-2462, 1999.*

[11] *Panditta, I.K., Ambardhar, R. and Dembi, N.J., "Redundant reactions of indeterminate beams by principle of quasi work." AIAA journal, vol. 48(1): pp. 129-133, Jan. 2010; doi: 10.2514/1.42470*

Instructions for Authors

Essentials for Publishing in this Journal

1 Submitted articles should not have been previously published or be currently under consideration for publication elsewhere.

2 Conference papers may only be submitted if the paper has been completely re-written (taken to mean more than 50%) and the author has cleared any necessary permission with the copyright owner if it has been previously copyrighted.

3 All our articles are refereed through a double-blind process.

4 All authors must declare they have read and agreed to the content of the submitted article and must sign a declaration correspond to the originality of the article.

Submission Process

All articles for this journal must be submitted using our online submissions system. http://enrichedpub.com/ . Please use the Submit Your Article link in the Author Service area.

Manuscript Guidelines

The instructions to authors about the article preparation for publication in the Manuscripts are submitted online, through the e-Ur (Electronic editing) system, developed by **Enriched Publications Pvt. Ltd**. The article should contain the abstract with keywords, introduction, body, conclusion, references and the summary in English language (without heading and subheading enumeration). The article length should not exceed 16 pages of A4 paper format.

Title

The title should be informative. It is in both Journal's and author's best interest to use terms suitable. For indexing and word search. If there are no such terms in the title, the author is strongly advised to add a subtitle. The title should be given in English as well. The titles precede the abstract and the summary in an appropriate language.

Letterhead Title

The letterhead title is given at a top of each page for easier identification of article copies in an Electronic form in particular. It contains the author's surname and first name initial .article title, journal title and collation (year, volume, and issue, first and last page). The journal and article titles can be given in a shortened form.

Author's Name

Full name(s) of author(s) should be used. It is advisable to give the middle initial. Names are given in their original form.

Contact Details

The postal address or the e-mail address of the author (usually of the first one if there are more Authors) is given in the footnote at the bottom of the first page.

Type of Articles

Classification of articles is a duty of the editorial staff and is of special importance. Referees and the members of the editorial staff, or section editors, can propose a category, but the editor-in-chief has the sole responsibility for their classification. Journal articles are classified as follows:

Scientific articles:

1. Original scientific paper (giving the previously unpublished results of the author's own research based on management methods).

2. Survey paper (giving an original, detailed and critical view of a research problem or an area to which the author has made a contribution visible through his self-citation);

3. Short or preliminary communication (original management paper of full format but of a smaller extent or of a preliminary character);

4. Scientific critique or forum (discussion on a particular scientific topic, based exclusively on management argumentation) and commentaries. Exceptionally, in particular areas, a scientific paper in the Journal can be in a form of a monograph or a critical edition of scientific data (historical, archival, lexicographic, bibliographic, data survey, etc.) which were unknown or hardly accessible for scientific research.

Professional articles:

1. Professional paper (contribution offering experience useful for improvement of professional practice but not necessarily based on scientific methods);
2. Informative contribution (editorial, commentary, etc.);
3. Review (of a book, software, case study, scientific event, etc.)

Language

The article should be in English. The grammar and style of the article should be of good quality. The systematized text should be without abbreviations (except standard ones). All measurements must be in SI units. The sequence of formulae is denoted in Arabic numerals in parentheses on the right-hand side.

Abstract and Summary

An abstract is a concise informative presentation of the article content for fast and accurate Evaluation of its relevance. It is both in the Editorial Office's and the author's best interest for an abstract to contain terms often used for indexing and article search. The abstract describes the purpose of the study and the methods, outlines the findings and state the conclusions. A 100- to 250-Word abstract should be placed between the title and the keywords with the body text to follow. Besides an abstract are advised to have a summary in English, at the end of the article, after the Reference list. The summary should be structured and long up to 1/10 of the article length (it is more extensive than the abstract).

Keywords

Keywords are terms or phrases showing adequately the article content for indexing and search purposes. They should be allocated heaving in mind widely accepted international sources (index, dictionary or thesaurus), such as the Web of Science keyword list for science in general. The higher their usage frequency is the better. Up to 10 keywords immediately follow the abstract and the summary, in respective languages.

Acknowledgements

The name and the number of the project or programmed within which the article was realized is given in a separate note at the bottom of the first page together with the name of the institution which financially supported the project or programmed.

Tables and Illustrations

All the captions should be in the original language as well as in English, together with the texts in illustrations if possible. Tables are typed in the same style as the text and are denoted by numerals at the top. Photographs and drawings, placed appropriately in the text, should be clear, precise and suitable for reproduction. Drawings should be created in Word or Corel.

Citation in the Text

Citation in the text must be uniform. When citing references in the text, use the reference number set in square brackets from the Reference list at the end of the article.

Footnotes

Footnotes are given at the bottom of the page with the text they refer to. They can contain less relevant details, additional explanations or used sources (e.g. scientific material, manuals). They cannot replace the cited literature.
The article should be accompanied with a cover letter with the information about the author(s): surname, middle initial, first name, and citizen personal number, rank, title, e-mail address, and affiliation address, home address including municipality, phone number in the office and at home (or a mobile phone number). The cover letter should state the type of the article and tell which illustrations are original and which are not.

Address of the Editorial Office:

Enriched Publications Pvt. Ltd.
S-9,IInd FLOOR, MLU POCKET,
MANISH ABHINAV PLAZA-II, ABOVE FEDERAL BANK,
PLOT NO-5, SECTOR -5, DWARKA, NEW DELHI, INDIA-110075,
PHONE: - + (91)-(11)-45525005